

Temperature dependence of spin to charge conversion in topological insulator/ferromagnet heterostructures



MASTER THESIS

written by
Alexander Glötzl
University of
Regensburg

supervised by
Prof. Dr. Christian Back

October 10, 2019

Contents

1	Introduction	1
2	Theory	2
2.1	Magnetic moment	2
2.2	Ferromagnetism	3
2.3	Energy density in a ferromagnet	4
2.3.1	Exchange energy	5
2.3.2	Demagnetization energy	5
2.3.3	Magnetic anisotropy	6
2.3.4	Zeeman energy	7
2.4	Time-dependence of the magnetisation vector	7
2.4.1	Landau-Lifschitz-Gilbert equation	7
2.4.2	Ferromagnetic resonance condition	8
2.4.2.1	Rotation of the coordinate system	9
2.4.2.2	Calculation of the effective field	9
2.4.2.3	Solution of linearized LLG	11
2.4.2.4	Resonance condition of FMR	12
2.4.2.5	Resonance line shape	13
2.5	Spin pumping	14
2.6	Voltages in a TI/Py heterostructure	16
2.6.1	Anisotropic magnetoresistance	16
2.6.2	Voltage generated by TI	17
3	Topological insulator	18
3.1	Integer quantum Hall state	18
3.2	Graphene	22
3.3	Quantum spin Hall state	26
3.4	Z_2 topological insulator	28
3.5	3D topological insulator	29
3.5.1	Weak topological insulator	29
3.5.2	Strong topological insulator	30
3.6	Charge to spin conversion	32
4	Experimental setup and processing of data	33
4.1	Experimental setup	33

Contents

4.2	Coplanar waveguide	35
4.3	Lithography	36
4.4	Processing the data	37
4.4.1	Evaluation and fit of resonance curve in FMR	37
4.4.2	Evaluation and fit of voltages	38
5	Experiments	41
5.1	Ferromagnetic Resonance	41
5.1.1	FMR in the cryostat	43
5.2	Angle dependence at room temperature	44
5.3	Temperature dependence at $\varphi_H = 45^\circ$	48
5.4	Temperature dependence at $\varphi_H = 0^\circ$	50
5.5	Angle dependence for Py/BSTS at room temperature and 10 Kelvin	51
6	Conclusion	53

1 Introduction

Since 1965 the computing power of microprocessor chips has been governed by Moore's law, which states that every two years the number of transistors on a silicon chip will double. However this law's exponential growth has come to falter in recent years since transistors have become so small that overheating through current leakage has become a problem [27]. A prominent solution to this problem could be the replacement of charge currents with spin currents. The idea is that information in computer components could be transferred through the orientation of the spin of an electron instead of its charge, which would cause no more heating.

In order to investigate ferromagnetic samples, ferromagnetic resonance (FMR) is a widely used tool in the research area of magnetism to obtain the damping constant α of a sample or to create a spin current. These spintronic elements however can only be useful if a reliable connection to classical electric components can be formed. Therefore a mechanism for converting charge currents into spin currents has to be developed.

In this thesis the properties of topological insulators are investigated, which behave as insulators in the bulk, but contain conducting surface states. These surface states of topological insulators could accomplish the afore mentioned conversion between charge and spin currents.

2 Theory

In this chapter a introduction into the basics of magnetism, relevant for understanding the discussion in later chapters, is given. First the magnetic moment and its properties are reviewed and then the different energies present in a ferromagnet are considered. The next chapter follows with the derivation of the Landau-Lifshitz-Gilbert equation. Afterwards the condition for ferromagnetic resonance and the magnetic susceptibility are calculated. Furthermore the process of spin pumping and the voltages along a heterostructure during FMR are discussed.

2.1 Magnetic moment

A fundamental quantity in magnetism is the magnetic moment \vec{m} . Classically it is described by an electric current I flowing around a closed area \vec{A} , where the length of \vec{A} is equal to the area of the loop [8] [6]. Then the magnetic moment is given by

$$\vec{m} = I\vec{A}. \quad (2.1)$$

This electric current consists of moving electrons with masses m_e and therefore magnetic moment can be connected to the angular momentum \vec{l} of these electrons [8]

$$\vec{m} = \gamma \vec{l}, \quad (2.2)$$

where γ is called the gyromagnetic ratio. The gyromagnetic ratio for an electron is $\gamma = -e/2m_e$.

Due to quantum mechanics, besides the angular momentum \vec{l} , the spin angular momentum \vec{s} has also to be considered. The magnetic moment then is described by [6]

$$\vec{m} = \frac{q}{2m} (g_l \vec{l} + g_s \vec{s}), \quad (2.3)$$

where q is charge, m is mass and g is called the Landé-Factor. For a free electron $g_l = 1$ and $g_s \approx 2$.

The magnetic moment of an electron in its ground state, that is circling a proton, is expressed by the physical constant μ_B , called Bohr magneton, and has the value of

$$\mu_B = \frac{q\hbar}{2m_e} \approx 9.274 \cdot 10^{-24} \text{ J T}^{-1}. \quad (2.4)$$

2.2 Ferromagnetism

Since the magnetic moment \vec{m} is a microscopic quantity describing a single particle, the introduction of a macroscopic quantity is needed. By dividing the magnetic moment $\Delta\vec{m}$ by volume ΔV , the magnetisation vector

$$\vec{M} = \frac{\Delta\vec{m}}{\Delta V} \quad (2.5)$$

is derived [6].

A magnetic moment \vec{m} in a magnetic field \vec{B} has the energy [3]

$$E = -\vec{m}\vec{B}. \quad (2.6)$$

Unlike with an electric dipole moment \vec{p} in an electric field \vec{E} , where a torque tends to align \vec{p} and \vec{E} , the angular momentum of a magnetic moment \vec{m} in a magnetic field \vec{B} causes a precession of \vec{m} around \vec{B} , as illustrated in 2.1.

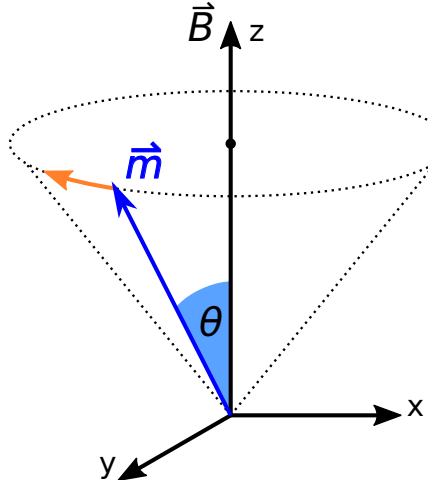


Figure 2.1: A magnetic moment \vec{m} in an external magnetic field \vec{B} precesses around the magnetic field at an angle θ at the Larmor precession frequency $\omega_{\text{Larmor}} = \gamma B$. Without damping the magnetic moment \vec{m} will precess infinitely. Figure taken from [3].

2.2 Ferromagnetism

Unlike in diamagnets and paramagnets, spontaneous magnetisation can occur in ferromagnets, even if no external magnetic field is present [11]. In this case all the magnetic moments \vec{m} are aligned parallel in the ferromagnet. Whether a metal is paramagnetic or ferromagnetic, depends on the interaction of the Coloumb potential and the kinetic energy of the spins. Spontaneous magnetisation can be achieved by shifting spin down

2 Theory

electrons near the Fermi edge into the spin up electron band and flipping their spin during the process. This process is depicted in figure 2.2. States with larger kinetic energy are now occupied in the spin up band and this shifting therefore costs kinetic energy. However the created positive net magnetisation creates a field, that interacts with the spins itself and lowers the energy cost of the process. This exchange of the spins is due to the Coulomb interaction. After calculating the total change of energy, $\Delta E = \Delta E_{\text{Kinetic}} + \Delta E_{\text{Potential}}$, the Stoner criterion is found [3].

$$Ug(E_F) \geq 1 \quad (2.7)$$

U is a measure for the exchange energy and $g(E_F)$ is the density of states at the Fermi energy. This criterion holds true for the 3d transition metals iron, cobalt and nickel since those have a high exchange interaction and the 3d bands are flat in \vec{k} -space, which results in large density of states near the Fermi edge.

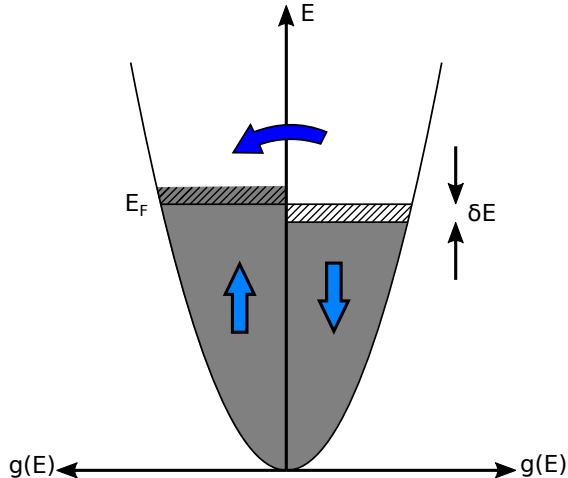


Figure 2.2: A large density of states near the Fermi edge can cause spontaneous energy band splitting without an external magnetic field. The amount of electrons transferred is $g(E_F)\delta E/2$ and their energy increases by δE . Figure taken from [3].

2.3 Energy density in a ferromagnet

In this chapter the most important energy contributions in a ferromagnet are presented. The total energy can be summed up in four terms [28],

$$\epsilon = \epsilon_{\text{ex}} + \epsilon_{\text{dem}} + \epsilon_{\text{ani}} + \epsilon_{\text{zee}}. \quad (2.8)$$

2.3.1 Exchange energy

In thin ferromagnetic layers all magnetic moments are approximately aligned parallel due to the exchange interaction. The magnetic configuration of the sample then can be described by a single magnetisation vector, hence the name macro-spin approximation is used. The first sum in equation 2.8 is called the exchange energy ϵ_{ex} and describes the energy corresponding to nonparallel alignment of the magnetic moments inside the sample. However, since the macro-spin approximation is used, the exchange energy is constant in a thin layered sample. Since a thin stripe of ferromagnetic material is considered within this thesis, the exchange energy ϵ_{ex} will no longer be regarded [11].

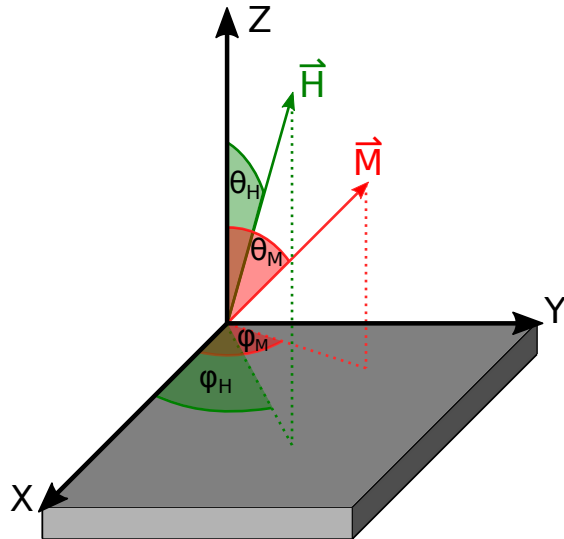


Figure 2.3: The spherical coordinate system, that was used for \vec{H} and \vec{M} and their respective angles φ and θ on top of a thin layered sample.

2.3.2 Demagnetization energy

One of Maxwell's equations states, that the magnetic field \vec{B} is solenoidal.

$$\vec{\nabla} \cdot \vec{B} = 0 \quad (2.9)$$

The magnetization \vec{M} is restricted to the ferromagnet and has to stop at the surface. This divergence of \vec{M} can be written as

$$\vec{\nabla} \cdot \vec{H} = -\vec{\nabla} \cdot \vec{M}, \quad (2.10)$$

with $\vec{B} = \mu_0 \vec{H} + \mu_0 \vec{M}$. Equation 2.10 states, that the magnetic field \vec{H} has an equal and opposite divergence of \vec{M} . This magnetic field is therefore called demagnetizing field H_d

2 Theory

because of its opposite direction to the external magnetic field \vec{H}_{ex} [3]. Figure 2.4 shows the demagnetizing field in a flat plate. The total magnetic field \vec{H} is then comprised of,

$$\vec{H} = \vec{H}_{\text{ex}} + \vec{H}_d = \vec{H}_{\text{ex}} - \mathcal{N}\vec{M}, \quad (2.11)$$

where \mathcal{N} is a demagnetizing tensor with $\text{Tr}(\mathcal{N}) = 1$. In thin layers the components

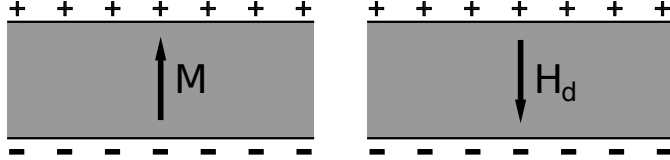


Figure 2.4: The figure shows the cross section of a thin sample plate. If the magnetization is perpendicular to the sample plane, there is a negative divergence of \vec{M} on the top surface, which creates a positive divergence of \vec{H} . This entails positive *magnetic charges* on the top surface, which produce the demagnetizing field \vec{H}_d in the opposite direction of \vec{M} . Figure taken from [3].

of the demagnetizing field along the width and length of the sample can be neglected because the *magnetic charges* are very far apart in comparison to the thickness of sample. Therefore $\mathcal{N}_{XX} = \mathcal{N}_{YY} = 0$ and $\mathcal{N}_{ZZ} = 1$.

The demagnetizing energy of a ferromagnetic sample is the energy the sample has in its own demagnetizing field. By changing the magnetisation by $d\vec{M}$ in an arbitrary magnetic field \vec{H} , the change in the density energy is

$$d\epsilon = -\mu_0 \vec{H} \cdot d\vec{M}. \quad (2.12)$$

By integrating $\vec{M} = M\hat{\vec{m}}$, with $\hat{\vec{m}}$ being the unit magnetization vector of \vec{M} , from 0 to saturation \vec{M}_S the following expression is obtained [11] [28]:

$$\epsilon_{\text{dem}} = \frac{1}{2} \mu_0 M_S^2 \hat{\vec{m}} (\mathcal{N} \hat{\vec{m}}) \quad (2.13)$$

2.3.3 Magnetic anisotropy

In a ferromagnetic certain orientations of the magnetisation \vec{M} can be energetically favored. This is called magnetic anisotropy and arises from spin-orbit interaction. The favored directions can be concluded from symmetry and structure of the crystal. Thus external field \vec{H} and magnetization \vec{M} are usually not parallel in a ferromagnet. The sample used in this thesis consists of permalloy (Py) and a topological insulator on top of a Al_2O_3 substrat and should show no anisotropy. However during the growth of the permalloy layer by sputtering, an uniaxial anisotropy can occur, that is perpendicular to the sample plane. The energy density can be calculated by [11]

$$\epsilon_{\text{ani}} = -K_U^\perp (m_Z^2). \quad (2.14)$$

2.4 Time-dependence of the magnetisation vector

K_U^\perp is a anisotropy constant (units: J m^{-3}) and m_Z is the z component of the unit magnetization vector $m_Z = M_Z/M$. This uniaxial anisotropy usually forms because of interface effects or strain between the layers of the sample.

2.3.4 Zeeman energy

A magnetized sample in an external magnetic field \vec{H}_{ex} has the energy given by [11]

$$\epsilon_{\text{zee}} = -\mu_0 M_S \vec{H}_{\text{ex}} \cdot \hat{\vec{m}}, \quad (2.15)$$

ϵ_{zee} is called Zeeman energy and is lowest when the magnetization \vec{M} are aligned parallel with the external magnetic field \vec{H}_{ex} .

2.4 Time-dependence of the magnetisation vector

So far the magnetization \vec{M} has been considered as time-independent. In this chapter the response of \vec{M} to an external perturbation will be discussed and this knowledge will then be used to derive the resonance condition of a ferromagnet in FMR.

2.4.1 Landau-Lifschitz-Gilbert equation

If the magnetization \vec{M} is perturbed from its equilibrium position by an external magnetic field \vec{H}_0 , the magnetization vector will start to precess around the effective field \vec{H}_{eff} in an elliptical orbit. The definition of H_{eff} will be explained in chapter 2.4.2.2. Damping in the sample causes the magnetization \vec{M} to rapidly return to its equilibrium position within a couple of nanoseconds [28]. In 1935 Landau and Lifschitz found a way to describe this behavior mathematically [14]. But only in 1955, when Gilbert added a different damping term to their equation, the time-dependent behaviour of \vec{M} was described correctly. Hence the equation is called Landau-Lifschitz-Gilbert (LLG) equation,

$$\frac{d\vec{m}}{dt} = -\gamma \mu_0 \vec{m} \times \vec{H}_{\text{eff}} + \alpha \vec{m} \times \frac{d\vec{m}}{dt}, \quad (2.16)$$

where α is a dimensionless constant called Gilbert damping factor, that shows the strength of damping in the sample, and $\vec{m} = \vec{M}/M_S$ is the unit magnetization vector [28].

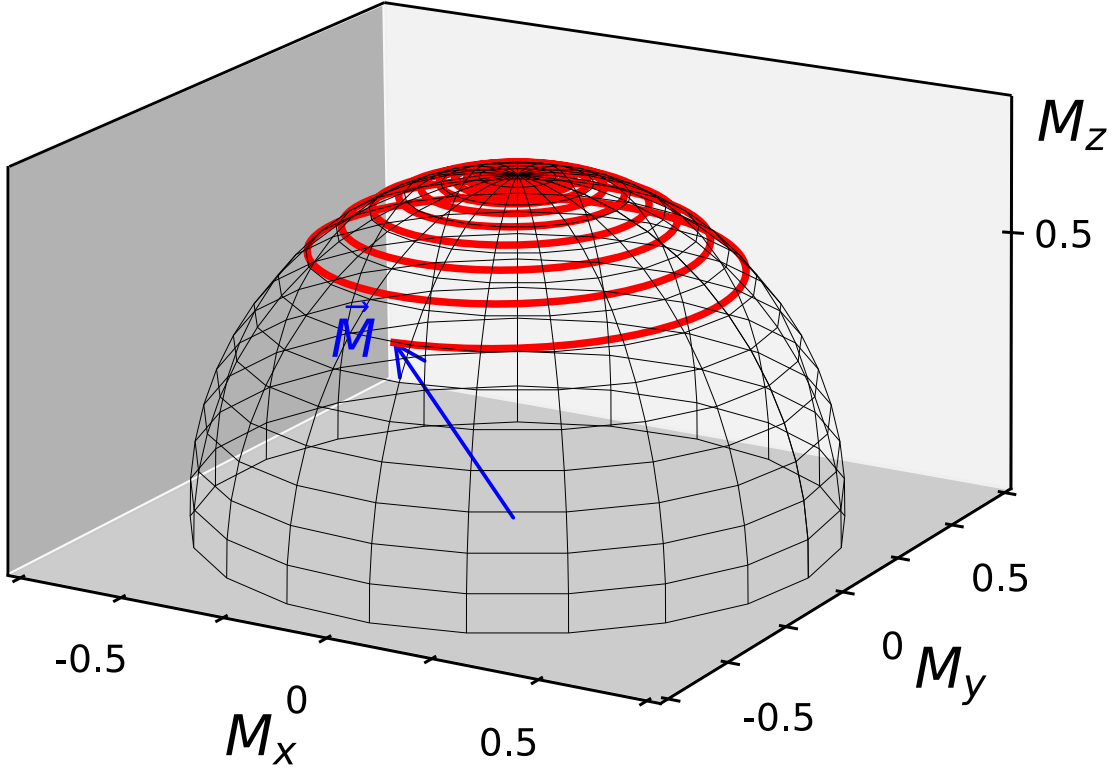


Figure 2.5: Solution of the LLG shows the path (red) of the magnetization \vec{M} describing a spiral motion to its equilibrium position for $\alpha = 0.05$, $\gamma = 200 \text{ GHz T}^{-1}$ and $\mu_0 M_S = 700 \text{ mT}$. The effective magnetic field $\vec{H}_{\text{eff}} = 1 \text{ T}$ and is pointing in the z-direction. The starting position of the magnetization \vec{M} is chosen to be in the yz-plane, $\vec{M} = \frac{1}{\sqrt{2}}(0, -\mu_0 M_S, \mu_0 M_S)$.

2.4.2 Ferromagnetic resonance condition

In an FMR-experiment the magnetization vector is excited by a high frequency magnetic field \vec{h} in the microwave wavelength region, which causes the magnetization \vec{M} to precess around the equilibrium position. The sample is located in an external static magnetic field \vec{H}_0 and the magnetization precesses around the effective magnetic field \vec{H}_{eff} . The high frequency magnetic field in the microwave wavelength is usually realized by a coplanar waveguide. A higher external magnetic field leads to a higher precession frequency since $\omega_{\text{Larmor}} = \gamma B$ and thus at a certain value of the external magnetic field $H_0 = H_{\text{FMR}}$ the sample can absorb some of the microwaves from the waveguide and a drop of microwave transmission can be measured. The evaluation of FMR measurements mainly consists of the determination of the line width ΔH and resonance position H_{FMR} of the measured curves, which can then be used to calculate the g factor or Gilbert damping factor α [16].

2.4 Time-dependence of the magnetisation vector

2.4.2.1 Rotation of the coordinate system

In order to make the following calculations easier it is recommended to transfer the current coordinate system XYZ into a new xyz coordinate system. In the new coordinate system the x axis is parallel to the magnetization \vec{M} . First the XYZ coordinate system is rotated by an angle φ_M in the XY plane and then the new intermediate x'y'z' coordinate system is tilted upwards by an angle $90^\circ - \theta_M$ along the y' axis. The transformation matrices from the old to the new coordinate system and vice versa are given by [20]

$$\begin{aligned} \begin{pmatrix} M_x \\ M_y \\ M_z \end{pmatrix} &= T_{XYZ}^{xyz} \begin{pmatrix} M_X \\ M_Y \\ M_Z \end{pmatrix} = \\ &= \begin{pmatrix} \sin \theta_M \cos \varphi_M & \sin \theta_M \sin \varphi_M & \cos \theta_M \\ -\sin \varphi_M & \cos \varphi_M & 0 \\ -\cos \theta_M \cos \varphi_M & -\cos \theta_M \sin \varphi_M & \sin \theta_M \end{pmatrix} \begin{pmatrix} M_X \\ M_Y \\ M_Z \end{pmatrix} \end{aligned} \quad (2.17)$$

A conversion from the new to the old coordinate system is given by the inverse of T_{XYZ}^{xyz}

$$\begin{aligned} \begin{pmatrix} M_X \\ M_Y \\ M_Z \end{pmatrix} &= T_{xyz}^{XYZ} \begin{pmatrix} M_x \\ M_y \\ M_z \end{pmatrix} = \\ &= \begin{pmatrix} \sin \theta_M \cos \varphi_M & -\sin \varphi_M & -\cos \theta_M \cos \varphi_M \\ \sin \theta_M \sin \varphi_M & \cos \varphi_M & -\cos \theta_M \sin \varphi_M \\ \cos \theta_M & 0 & \sin \theta_M \end{pmatrix} \begin{pmatrix} M_x \\ M_y \\ M_z \end{pmatrix} \end{aligned} \quad (2.18)$$

2.4.2.2 Calculation of the effective field

In FMR the magnetization precesses around the effective magnetic field \vec{H}_{eff} . As shown in chapter 2.3 the total energy density is [28] [16]

$$\epsilon = \frac{1}{2} \mu_0 M_S^2 m_Z^2 - K_U^\perp m_Z^2 - \mu_0 M_S \vec{H}_{\text{ex}} \cdot \vec{m}. \quad (2.19)$$

The equilibrium position of \vec{M} is given by minimizing the total density energy under the condition that the absolute value of the magnetization does not change $|\vec{M}|^2 = 1$. By expressing \vec{m} and \vec{H}_{ex} in spherical coordinates and differentiating with respect to θ_M and φ_M and setting both equations to 0 the following two equations are obtained [16]:

$$M_{\text{eff}} \cos \theta_M \sin \theta_M + H_0 \sin(\theta_H - \theta_M) = 0 \quad (2.20)$$

$$\varphi_H = \varphi_M \quad (2.21)$$

2 Theory

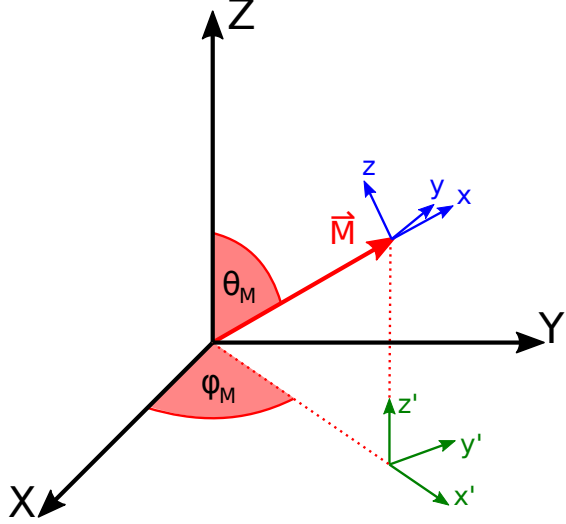


Figure 2.6: Transition from the XYZ coordinate system to the new xyz coordinate system. First the XYZ coordinate system is rotated in the XY-plane and then rotated along the intermediate axis y' .

Two trigonometric functions¹ were used in (2.20)-(2.21) and

$$M_{\text{eff}} = M_S - \frac{2K_U^\perp}{\mu_0 M_S}, \quad (2.22)$$

was introduced. The effective magnetic field \vec{H}_{eff} is then calculated by taking the gradient of the total energy density of a thin sample with respect to the coordinates of the magnetization \vec{M} [16]

$$\mu_0 \vec{H}_{\text{eff}} = -\frac{1}{M_S} \vec{\nabla}_{\vec{m}} \epsilon. \quad (2.23)$$

The effective field has to be transferred into the coordinate system xyz. This is done by using equation 2.17, $\mu_0 \vec{H}_{\text{eff}} = T_{XYZ}^{xyz}(\mu_0 \vec{H}_{\text{eff}})$:

$$\mu_0 H_{\text{eff},x} = \mu_0 \sin \theta_M \cos \varphi_M H_{\text{ex},X} + \mu_0 \sin \theta_M \sin \varphi_M H_{\text{ex},Y} + \quad (2.24)$$

$$\mu_0 \cos \theta_M H_{\text{ex},Z} - \mu_0 \cos \theta_M M_{\text{eff}} m_Z$$

$$\mu_0 H_{\text{eff},y} = -\mu_0 \sin \varphi_M H_{\text{ex},X} + \mu_0 \cos \varphi_M H_{\text{ex},Y} \quad (2.25)$$

$$\mu_0 H_{\text{eff},z} = \mu_0 \cos \theta_M \cos \varphi_M H_{\text{ex},X} + \mu_0 \cos \theta_M \sin \varphi_M H_{\text{ex},Y} + \quad (2.26)$$

$$\mu_0 \sin \theta_M H_{\text{ex},Z} - \mu_0 \sin \theta_M M_{\text{eff}} m_Z$$

Next $m_Z = \cos \theta_M m_x + \sin \theta_M m_z$ is inserted into equation (2.24) and (2.26). The external magnetic field \vec{H}_{ex} can be split into a static external magnetic field \vec{H}_0 and a

¹ $\sin(\theta_H - \theta_M) = \cos \theta_M \sin \theta_H - \cos \theta_H \sin \theta_M$
 $\sin(\varphi_H - \varphi_M) = \sin \varphi_H \cos \varphi_M - \cos \varphi_H \sin \varphi_M$

2.4 Time-dependence of the magnetisation vector

small microwave magnetic field \vec{h} with frequency ω [16] [5].

$$\vec{H}_{\text{ex}} = \begin{pmatrix} H_0 \sin \theta_H \cos \varphi_H \\ H_0 \sin \theta_H \sin \varphi_H \\ H_0 \cos \theta_H \end{pmatrix} + \vec{h} \exp(iwt) \quad (2.27)$$

Inserting equation (2.27) into (2.24)-(2.26) results in:

$$\begin{aligned} \mu_0 H_{\text{eff},x} &= \mu_0 H_0 (\sin \theta_M \sin \theta_H \cos(\varphi_H - \varphi_M) + \cos \theta_M \cos \theta_H) \\ &\quad - \mu_0 M_{\text{eff}} \cos \theta_M (\cos \theta_M m_x + \sin \theta_M m_z) + \mu_0 h_x \exp(iwt) \end{aligned} \quad (2.28)$$

$$\mu_0 H_{\text{eff},y} = \mu_0 H_0 \sin \theta_M \sin(\varphi_H - \varphi_M) + \mu_0 h_y \exp(iwt) \quad (2.29)$$

$$\begin{aligned} \mu_0 H_{\text{eff},z} &= \mu_0 H_0 (-\cos \theta_M \sin \theta_H \cos(\varphi_H - \varphi_M) + \sin \theta_M \cos \theta_H) \\ &\quad - \mu_0 M_{\text{eff}} \sin \theta_M (\cos \theta_M m_x + \sin \theta_M m_z) + \mu_0 h_z \exp(iwt) \end{aligned} \quad (2.30)$$

After the assumption of a rather small magnetic microwave field, that only leads to very small oscillations of the magnetization $m_x \approx 1$ and $m_y, m_z \ll 1$ can be used. After applying the calculated equilibrium position of \vec{M} , stated in equation (2.20) and (2.21), the effective field can be further simplified [16]:

$$\begin{aligned} \mu_0 H_{\text{eff},x} &= \mu_0 H_0 \cos(\theta_H - \theta_M) - \mu_0 M_{\text{eff}} \cos \theta_M (\cos \theta_M m_x + \sin \theta_M m_z) \\ &\quad + \mu_0 h_x \exp(iwt) \end{aligned} \quad (2.31)$$

$$\mu_0 H_{\text{eff},y} = \mu_0 h_y \exp(iwt) \quad (2.32)$$

$$\mu_0 H_{\text{eff},z} = -\mu_0 M_{\text{eff}} \sin^2 \theta_M m_z + \mu_0 h_z \exp(iwt) \quad (2.33)$$

In equation (2.31) a trigonometric function² was used and equation (2.33) made particular use of equation (2.20).

2.4.2.3 Solution of linearized LLG

The oscillation of the magnetization \vec{M} is described by the Landau-Lifschitz-Gilbert equation (2.16). In general an analytic solution is not possible because the LLG is a nonlinear differential equation. However for small excitation fields \vec{h} a linearization ansatz can be made for the unit magnetization vector:

$$\vec{m} = \begin{pmatrix} 1 \\ m_y \exp(iwt) \\ m_z \exp(iwt) \end{pmatrix} \quad (2.34)$$

Combining equation (2.34) with the LLG (2.16) and neglecting all quadratic orders of m_y and m_z results in [16]:

$$m_y = -\gamma \mu_0 (m_z H_{\text{eff},x} - H_{\text{eff},z}) - \alpha(i\omega) m_z \quad (2.35)$$

$$m_z = -\gamma \mu_0 (H_{\text{eff},y} - m_y H_{\text{eff},x}) + \alpha(i\omega) m_y \quad (2.36)$$

² $\cos(\theta_H - \theta_M) = \sin \theta_M \sin \theta_H + \cos \theta_M \cos \theta_H$

2 Theory

The components of the effective field \vec{H}_{eff} can then be replaced by equations (2.31)-(2.33). Here also the quadratic orders of \mathbf{m}_y and \mathbf{m}_z or mix terms between components of \vec{h} and \mathbf{m}_y (or \mathbf{m}_z) can be neglected.

$$0 = i\frac{\omega}{\gamma} \mathbf{m}_y + \left(\mathfrak{B}_{\text{eff}} + \alpha i\frac{\omega}{\gamma} \right) \mathbf{m}_z - \mu_0 h_z \quad (2.37)$$

$$0 = -i\frac{\omega}{\gamma} \mathbf{m}_z + \left(\mu_0 \mathfrak{H}_{\text{eff}} + \alpha i\frac{\omega}{\gamma} \right) \mathbf{m}_y - \mu_0 h_y \quad (2.38)$$

Above the effective magnetic induction $\mathfrak{B}_{\text{eff}}$ and the effective magnetic field $\mathfrak{H}_{\text{eff}}$ were introduced, where again the use of trigonometric functions³ has been made:

$$\mathfrak{B}_{\text{eff}} = \mu_0 H_0 \cos(\theta_H - \theta_M) - \mu_0 M_{\text{eff}} \cos 2\theta_M \quad (2.39)$$

$$\mu_0 \mathfrak{H}_{\text{eff}} = \mu_0 H_0 \cos(\theta_H - \theta_M) - \mu_0 M_{\text{eff}} \cos^2 \theta_M \quad (2.40)$$

2.4.2.4 Resonance condition of FMR

If the external magnetic field H_0 is increased, the magnetization will be in resonance at some value of H_0 , namely H_{FMR} . Then the amplitudes \mathbf{m}_y and \mathbf{m}_z of the magnetization unit vector will be maximized. By solving equations (2.37) and (2.38) for \mathbf{m}_y and \mathbf{m}_z ,

$$\mathbf{m}_y = \frac{-(\mathfrak{B}_{\text{eff}} + \frac{i\omega}{\gamma})\mu_0 h_y - \frac{i\omega}{\gamma} \mu_0 h_z}{\frac{\omega^2}{\gamma^2} - (\mu_0 \mathfrak{H}_{\text{eff}} + \frac{i\omega}{\gamma})(\mathfrak{B}_{\text{eff}} + \frac{i\omega}{\gamma})} \quad (2.41)$$

$$\mathbf{m}_z = \frac{-(\mu_0 \mathfrak{H}_{\text{eff}} + \frac{i\omega}{\gamma})\mu_0 h_z + \frac{i\omega}{\gamma} \mu_0 h_y}{\frac{\omega^2}{\gamma^2} - (\mu_0 \mathfrak{H}_{\text{eff}} + \frac{i\omega}{\gamma})(\mathfrak{B}_{\text{eff}} + \frac{i\omega}{\gamma})}, \quad (2.42)$$

The maximum of \mathbf{m}_y and \mathbf{m}_z is determined by minimizing the denominator so that

$$\left(\frac{\omega}{\gamma} \right)^2 = \mu_0 \mathfrak{B}_{\text{eff}} \mathfrak{H}_{\text{eff}} \Big|_{H_0=H_{\text{FMR}}} \quad (2.43)$$

Later experiments will be conducted in the in-plane configuration, where magnetization \vec{M} and external magnetic field \vec{H}_0 are in the sample plain, thus $\theta_H = \theta_M = 90^\circ$. The resonance condition (2.43) then simplifies to:

$$\left(\frac{\omega}{\gamma} \right)^2 = \mu_0 H_{\text{FMR}} (\mu_0 H_{\text{FMR}} + \mu_0 M_{\text{eff}}) \quad (2.44)$$

This resonance condition was first discovered by C. Kittel in 1948 and was therefore named the Kittel formula [16] [13].

³ $\cos 2\theta_M = \cos^2 \theta_M - \sin^2 \theta_M$

2.4 Time-dependence of the magnetisation vector

2.4.2.5 Resonance line shape

It can be proven that the imaginary part of the dynamic susceptibility is proportional to the microwave absorption of \vec{h} at resonance [16] [28]. So in order to find the line shape of the absorption curve, the dynamic susceptibility has to be calculated first. The dynamic susceptibility χ is defined by:

$$\vec{m} = \chi \vec{h}, \quad (2.45)$$

where χ is a tensor. By considering that h_x does not play a role in the excitation of the magnetization \vec{M} in the sample since they are both parallel to each other, χ can be expressed as:

$$\begin{pmatrix} m_y \\ m_z \end{pmatrix} = \begin{pmatrix} \chi_{yy} & \chi_{yz} \\ \chi_{zy} & \chi_{zz} \end{pmatrix} \begin{pmatrix} h_y \\ h_z \end{pmatrix} \quad (2.46)$$

By comparing equation 2.46 with the solutions for m_y and m_z (equation (2.41) and (2.42)) the components of the susceptibility tensor can be determined [16]:

$$\chi_{yy} = \frac{-(\mathfrak{B}_{\text{eff}} + \frac{i\alpha\omega}{\gamma})\mu_0}{(\frac{\omega}{\gamma})^2 - (\mu_0\mathfrak{H}_{\text{eff}} + \frac{i\alpha\omega}{\gamma})(\mathfrak{B}_{\text{eff}} + \frac{i\alpha\omega}{\gamma})} \quad (2.47)$$

$$\chi_{yz} = -\chi_{zy} = \frac{-\frac{i\omega}{\gamma}\mu_0}{(\frac{\omega}{\gamma})^2 - (\mu_0\mathfrak{H}_{\text{eff}} + \frac{i\alpha\omega}{\gamma})(\mathfrak{B}_{\text{eff}} + \frac{i\alpha\omega}{\gamma})} \quad (2.48)$$

$$\chi_{zz} = \frac{-(\mu_0\mathfrak{H}_{\text{eff}} + \frac{i\alpha\omega}{\gamma})\mu_0}{(\frac{\omega}{\gamma})^2 - (\mu_0\mathfrak{H}_{\text{eff}} + \frac{i\alpha\omega}{\gamma})(\mathfrak{B}_{\text{eff}} + \frac{i\alpha\omega}{\gamma})} \quad (2.49)$$

In order to calculate χ_{yy} explicitly, $\mathfrak{B}_{\text{eff}}$ and $\mathfrak{H}_{\text{eff}}$ are expanded to the first order of the taylor series near the resonance field H_{FMR} .

$$\mathfrak{B}_{\text{eff}} = \mathfrak{B}_{\text{FMR}} + \frac{\partial \mathfrak{B}_{\text{eff}}}{\partial H_0} \Big|_{H_0=H_{\text{FMR}}} \cdot \delta H + \mathcal{O}(\delta H^2) \quad (2.50)$$

$$\mu_0\mathfrak{H}_{\text{eff}} = \mu_0\mathfrak{H}_{\text{FMR}} + \mu_0 \frac{\partial \mathfrak{H}_{\text{eff}}}{\partial H_0} \Big|_{H_0=H_{\text{FMR}}} \cdot \delta H + \mathcal{O}(\delta H^2) \quad (2.51)$$

Here the effective magnetic fields at resonance $\mathfrak{B}_{\text{FMR}} = \mathfrak{B}_{\text{eff}} \Big|_{H_0=H_{\text{FMR}}}$ and $\mu_0\mathfrak{H}_{\text{FMR}} = \mu_0\mathfrak{H}_{\text{eff}} \Big|_{H_0=H_{\text{FMR}}}$ were introduced along with $\delta H = (H_0 - H_{\text{FMR}})$. Also it will be useful for the future to introduce the definition of line width $\mu_0\Delta H = \frac{\alpha\omega}{\gamma}$. The first order approximation of $\mathfrak{B}_{\text{eff}}$ and $\mathfrak{H}_{\text{eff}}$ can be used in (2.47) and the resulting term can be simplified by neglecting terms that are proportional to $\alpha\delta H$, α^2 or δH^2 and replacing $(\frac{\omega}{\gamma})^2$ by the resonance condition (2.43).

$$\chi_{yy} = \frac{(\mathfrak{B}_{\text{FMR}} + \frac{\partial \mathfrak{B}_{\text{eff}}}{\partial H_0} \Big|_{H_0=H_{\text{FMR}}} \cdot \delta H + i\mu_0\Delta H)\mu_0}{(\mathfrak{B}_{\text{FMR}} + \mu_0\mathfrak{H}_{\text{FMR}})i\mu_0\Delta H + (\mathfrak{B}_{\text{FMR}} \frac{\partial \mathfrak{H}_{\text{eff}}}{\partial H_0} \Big|_{H_0=H_{\text{FMR}}} + \mathfrak{H}_{\text{FMR}} \frac{\partial \mathfrak{B}_{\text{eff}}}{\partial H_0} \Big|_{H_0=H_{\text{FMR}}})\mu_0\delta H} \quad (2.52)$$

2 Theory

The derivation in (2.52) can be calculated by using equations (2.39) and (2.40) in the in-plane configuration ($\theta_H = \theta_M = 90^\circ$). Afterwards the result is multiplied by the complex conjugate of the denominator and the final result is:

$$\chi_{yy} = \frac{\mathfrak{B}_{\text{FMR}}}{(\mathfrak{B}_{\text{FMR}} + \mu_0 \mathfrak{H}_{\text{FMR}}) \Delta H} \left(\frac{\Delta H \delta H - i \Delta H^2}{\delta H^2 + \Delta H^2} + \frac{\mu_0 \Delta H}{\mathfrak{B}_{\text{FMR}}} \right) \quad (2.53)$$

The real part of χ_{yy} is an antisymmetric Lorentzian line shape with an offset, which can usually be neglected because $\mathfrak{B}_{\text{FMR}} \gg \mu_0 \Delta H$. The imaginary part resembles a symmetric Lorentzian line shape. As already stated in the beginning of this section the absorbed microwave power is proportional to the imaginary part of χ_{yy} and χ_{zz} . The mean absorbed power is given by [16]

$$\bar{P} = \frac{1}{2} \mu_0 M_S \omega (\text{Im}(\chi_{yy}) h_y^2 + \text{Im}(\chi_{zz}) h_z^2) \quad (2.54)$$

Thus the resonance curve in FMR measurements has a symmetric Lorentzian line shape. The derivation of χ_{zz} is analogous to the derivation of χ_{yy} .

2.5 Spin pumping

In a topological insulator/ferromagnet heterostructure spin momentum can be transferred from the ferromagnet to the topological insulator. In FMR the precession of the magnetic moments \vec{m} in the ferromagnet can accumulate spin momenta on the interface between topological insulator and ferromagnet. These spin momenta can diffuse into the surface states (see chapter 3) of the topological insulator [28]. Through spin-momentum locking a voltage can be measured at the ends of the topological insulator (see figure 2.7).

In scattering theory the spin current is described as follows [26] [25] [18],

$$I_{s, \text{pump}} \vec{s} = \frac{\hbar}{4\pi} A_r \hat{\vec{m}} \times \frac{\hat{\vec{m}}}{dt}, \quad (2.55)$$

with the unit magnetic vector $\hat{\vec{m}}$ in the ferromagnetic layer, the polarisation direction of the pumped spins \vec{s} , the absolute value of the pumped spin $I_{s, \text{pump}}$ and the conductivity of spin pumping A_r . The spin current is perpendicular to the interface of ferromagnet and topological insulator. The total pumped spin current however differs from the initially pumped spin current because a part of this spin current flows back from the topological insulator into the ferromagnet [26] [25].

$$I_{s,0} \vec{s} = (I_{s,\text{pump}} - I_{s,\text{back}}) \vec{s} = \frac{\hbar}{4\pi} \bar{A}_r \hat{\vec{m}} \times \frac{\hat{\vec{m}}}{dt}, \quad (2.56)$$

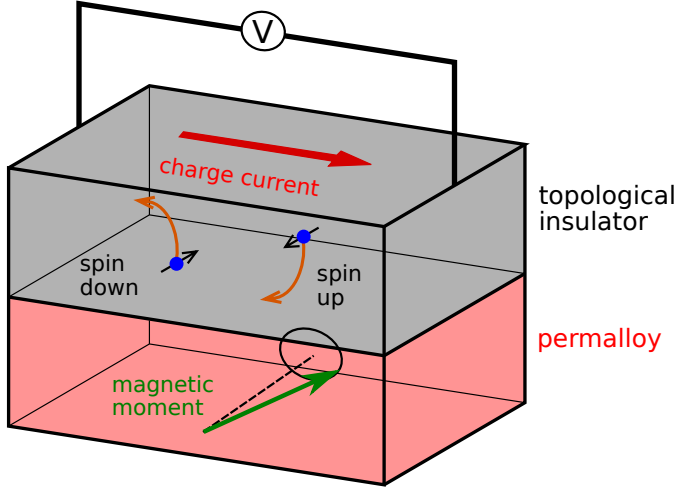


Figure 2.7: A topological/ferromagnet heterostructure can show conversion of spin current into charge current by spin pumping in FMR. Since opposite spins accumulate on the top and bottom surfaces, the charge current can be measured at the ends of the topological insulator layer because of spin-momentum locking in the surface states of the TI. Figure adapted from [22].

where \bar{A}_r is a modified spin pumping conductivity due to the backflow of spin [26]. Since the ferromagnetic layer loses spin momentum a continuity equation can be formed [28],

$$\frac{d\vec{S}}{dt} = -\vec{I}_s. \quad (2.57)$$

Using $\vec{m} = -\gamma\vec{S}$ the total spin \vec{S} in equation 2.57 can be replaced. After dividing by the volume of the ferromagnetic layer V_{FM} the result reads:

$$\frac{d\vec{M}}{dt} = \frac{\gamma}{V_{FM}}\vec{I}_s, \quad (2.58)$$

Here the spin current \vec{I}_s can be replaced with the result of equation 2.56 [26] [25] [28],

$$\frac{d\vec{M}}{dt} = \frac{\gamma\hbar A'_r}{4\pi V_{FM} M_S^2} \vec{M} \times \frac{d\vec{M}}{dt} = \frac{\alpha'}{M_S} \vec{M} \times \frac{d\vec{M}}{dt}. \quad (2.59)$$

This equation has the form of a damping term in the LLG (2.16) with a new damping parameter α' . The total damping parameter α therefore amounts to,

$$\alpha = \alpha_0 + \alpha', \quad (2.60)$$

where α_0 is the already discussed intrinsic damping parameter. Since α' can only be positive the total damping parameter increases through spin pumping [28].

2 Theory

2.6 Voltages in a TI/Py heterostructure

This chapter briefly discusses the different origins of the voltages measured in a permalloy/topological insulator heterostructure. There are mainly two voltages to be considered and they both change with the angle φ_H , at which the external magnetic field \vec{H}_0 is directed inside the sample stripe.

2.6.1 Anisotropic magnetoresistance

In a ferromagnetic sample the resistance depends on the angle between the current flowing through the ferromagnet and the magnetization of the sample. If the magnetization is perpendicular to the current flow the resistance shows a minimum R_0 . If magnetization is parallel to the direction of the current the total resistance R is increased by an amount of R_A [6]. Between maximal and minimal resistance the following relation is given [2],

$$R = R_0 + R_A \cos^2(\theta) \quad (2.61)$$

The voltage V_{AMR} can be calculated by the product of current in the ferromagnet and the resistance R . In an FMR-experiment induction or capacitive coupling induce a high-frequency alternating current $I_1 \cos(\omega t)$ in the sample stripe, where ω is the microwave frequency current in the coplanar waveguide. Since the magnetic moments precess with the frequency ω , the resistance R also oscillates with the same frequency. Overall the voltage due to AMR has a DC component, which is given by [2]

$$V_{\text{AMR}} = \frac{R_A I_1 \chi_{yz}^{\text{res}} h_{\text{rf}}}{2M_S} \left(\frac{\Delta H^2 \cos(\varphi_I)}{(H_0 - H_{\text{FMR}})^2 + \Delta H^2} - \frac{(H_0 - H_{\text{FMR}}) \sin(\varphi_I)}{(H_0 - H_{\text{FMR}})^2 + \Delta H^2} \right) \sin(2\varphi_H). \quad (2.62)$$

φ_I is the phase difference between magnetization and the alternating current in the ferromagnetic layer under resonance conditions. From equation 2.62 it can be seen that V_{AMR} has both a symmetric and an antisymmetric Lorentzian line shape.

2.6.2 Voltage generated by TI

As will be shown in the upcoming chapter 3 when spin is injected into the topological insulator, the spin-momentum locking results in a charge current along the "Hall" direction on the surface state. This voltage has a symmetric Lorentzian line shape and is proportional to $\cos \varphi_H$.

3 Topological insulator

Topological insulators (TI) are insulators with an ordinary bulk band gap but due to spin-orbit interaction and time-reversal symmetry topologically protected conducting states exist on the surface [12]. This chapter is a short introduction to topological band theory, where topological order and the underlying symmetries in a topological insulator are reviewed. Firstly the topology of the integer quantum Hall effect is discussed because much like the TI it has unique edge states, that can be distinguished from an ordinary insulator by the Chern invariant.

3.1 Integer quantum Hall state

The integer quantum Hall state occurs when electrons are confined to two dimensions in a strong magnetic field. The quantization of the cyclotron orbits of the electrons leads to the so called Landau levels. The energy of the Landau levels can be calculated by

$$\epsilon = \hbar\omega_c(n + 1/2), \quad (3.1)$$

where $\omega_c = \frac{-eB}{mc}$ is the cyclotron frequency and n is an integer. If n Landau levels are filled and the rest is empty (see figure 3.1), then an energy gap separates the occupied and the empty states just like in an insulator. In the integer quantum Hall state an electric field causes the cyclotron orbits to drift, leading to a quantized Hall conductivity [3],

$$\sigma_{xy} = \frac{ne^2}{h} \quad (3.2)$$

The quantized Hall conductivity can be measured in experiments with a very high precision. The Hall conductivity σ_{xy} is connected to the topology of the system, so as long as a perturbation is not sufficiently strong to change the topology of the sample the conductivity stays very robust and precise [12] .

In general, translation symmetry allows the single particle states to be labeled by their crystal momentum \vec{k} . With a magnetic field the generators of translation do not commute with one another and thus electronic states cannot be labeled with momentum. However, if a unit cell with area $2\pi\hbar c/eB$ enclosing a flux quantum is defined, then

3 Topological insulator

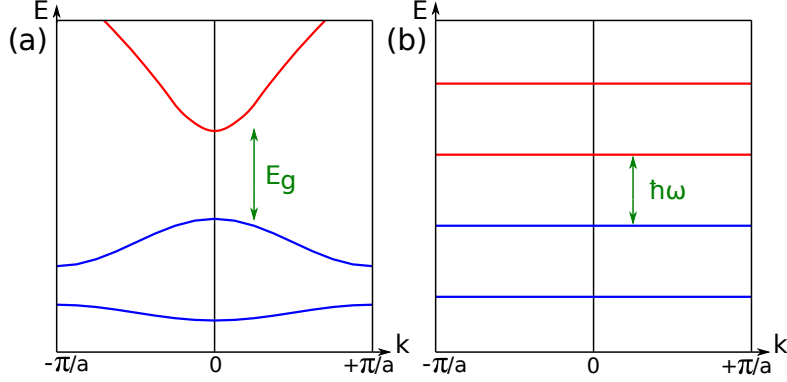


Figure 3.1: (a) The band structure of an insulator and in comparison (b) the Landau levels of a 2D electron gas in a magnetic field B . The Landau levels can be viewed as a band structure, where $E_g = \hbar\omega$ separates the occupied and the unoccupied states. Figure taken from [12]

lattice translations do commute and Bloch's theorem allows states to be labeled by 2D crystal momentum \vec{k} . According to Bloch's theorem these states can be written as

$$|\psi\rangle = \exp^{i\vec{k}\cdot\vec{r}}|u(\vec{k})\rangle, \quad (3.3)$$

where $|u(\vec{k})\rangle$ is a cell periodic eigenstate of the Bloch Hamiltonian,

$$H(\vec{k}) = \exp^{i\vec{k}\cdot\vec{r}} H \exp^{-i\vec{k}\cdot\vec{r}}. \quad (3.4)$$

The eigenvalues $E_n(\vec{k})$ define the band structure of the crystal. Due to lattice translation symmetry the relation $H(\vec{k} + \vec{G}) = H(\vec{k})$ can be used, where \vec{G} is the reciprocal lattice vector. It follows that the crystal momentum is defined in the periodic Brillouin zone, which has the topology of a torus T^d in d dimensions. A 2D band structure consists of a mapping from the crystal momentum \vec{k} , defined on a torus, to the Bloch Hamiltonian $H(\vec{k})$ [12].

Topological equivalence means the process of deforming systems into each other continuously. For example a torus cannot be transformed into a sphere continuously without closing the hole (figure 3.2). A theorem by Gauss and Bonnet states that the integral of the Gaussian curvature K over a closed surface is a quantized topological invariant, called the Euler characteristic χ . The Euler characteristic is related to the genus g (number of holes) by

$$\chi = 2 - 2g = \frac{1}{2\pi} \int_S K dA, \quad (3.5)$$

where $K = 1/R^2$ for a sphere with radius R . It follows that for a sphere $g = 0$ and for a torus $g = 1$. The genus g is a quantized topological invariant and originates from the integral over the Gaussian curvature [15]. In the following section the Chern number will be introduced as another topological invariant number. The Chern number originates

3.1 Integer quantum Hall state

from the integral over the Berry curvature.

In condensed matter physics topological equivalence can be explained by considering Hamiltonians of a system. Hamiltonians $H(\vec{k})$ can always be transformed into each other if there is no energy gap. With an energy gap however the Hamiltonians can be classified topologically into Hamiltonians $H(\vec{k})$ that can and cannot be transformed into each other without closing the energy gap. For example a Hamiltonian $H(\alpha)$ can be varied by an external parameter α , e.g. a gate voltage, into a different Hamiltonian H' [1],

$$H(\alpha) = \alpha H' + (1 - \alpha)H. \quad (3.6)$$

If an energy band crosses zero energy (see figure 3.2 (a)), H and H' are not topologically equivalent for this particular chosen path α . This does not mean that there is no transformation between H and H' that does not close the energy gap. In figure 3.2 (b) the energy gap closes twice. However it is not hard to imagine that by pushing the bound states down a bit and out of the energy gap a continuous transformation without energy gap closing can be achieved [12].

It is therefore useful to define a topological invariant $n \in \mathbb{Z}$ that clearly distinguishes the two classes.

The Berry phase is a phase difference acquired over the course of a cycle, when a system changes adiabatically. Usually some sort of singularity or hole in the topology is required to achieve a nontrivial ($\gamma_C \neq 1$) phase difference when going around a cycle. The Bloch states are invariant to this phase ambiguity [4],

$$|u(\vec{k})\rangle \rightarrow \exp^{i\phi(\vec{k})} |u(\vec{k})\rangle. \quad (3.7)$$

The Berry phase is defined as

$$\gamma_C = \oint_C \vec{A} \cdot d\vec{k} = \int_S \mathcal{F} d^2\vec{k}, \quad (3.8)$$

where $A = -i\langle u(\vec{k}) | \nabla_{\vec{k}} | u(\vec{k}) \rangle$ is called the Berry connection and $\mathcal{F} = \nabla \times A$ is called Berry curvature. The Berry phase can be approached graphically by choosing a two level Hamiltonian $H(\vec{k})$, which may be expressed by Pauli matrices $\vec{\sigma}$,

$$H(\vec{k}) = \vec{d}(\vec{k}) \cdot \vec{\sigma} = \begin{pmatrix} d_z & d_x - id_y \\ d_x + id_y & -d_z \end{pmatrix}. \quad (3.9)$$

This Hamiltonian has eigenvalues $\pm|\vec{d}|$, so that \vec{d} can be viewed as a point on a sphere S^2 (see figure 3.3). Berry was able to show, that for a closed loop C the phase associated with the ground state is [4]

$$\gamma_C = \frac{1}{2} \left(\text{Solid angle swept out by } \hat{\vec{d}}(\vec{k}) \right). \quad (3.10)$$

3 Topological insulator

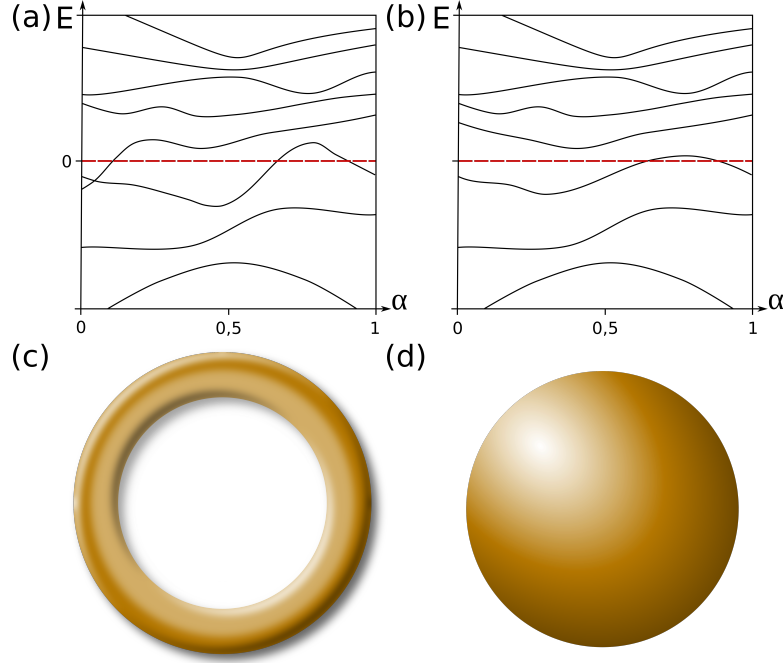


Figure 3.2: Different examples of band structures, that change by an external parameter α . The original Hamiltonian H starts at $\alpha = 0$ and is transformed into H' at $\alpha = 1$. (a) Continuous transformation can not be achieved for this particular path α because the energy gap closes. (b) Continuous transformation between H and H' can be achieved by pushing the bound states out of the energy gap without closing the energy gap. (c) A torus cannot be transformed continuously into (d) a sphere without closing the *hole*. Figure (a) and (b) taken from [1].

With equation 3.8 the Berry curvature is given by the solid angle per unit area in \vec{k} space,

$$\mathcal{F}_{\parallel} = \frac{1}{2} \epsilon_{ijk} \hat{\vec{d}} \cdot (\partial_i \hat{\vec{d}} \times \partial_j \hat{\vec{d}}). \quad (3.11)$$

The Berry curvature integrated over a closed 2D space is a multiple of 2π that is equal to the number of times $\hat{\vec{d}}$ wraps around the sphere as a function of \vec{k} . This gives rise to the Chern invariant number n , for a closed surface S .

$$n = \frac{1}{2} \int_S \mathcal{F} d^2 \vec{k}. \quad (3.12)$$

In a crystal the Chern invariant is the total Berry curvature \mathcal{F} over the Brillouin zone, where the sum over all occupied bands is again invariant

$$n = \sum_{m=1}^N n_m = \sum_{m=1}^N \frac{1}{2\pi} \int d^2 \vec{k} \mathcal{F}_m. \quad (3.13)$$

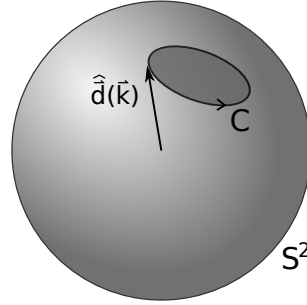


Figure 3.3: In a two band model the Berry phase can be understood as the solid angle swept out by \hat{d} along a cycle C on a sphere S^2 . Figure taken from [4].

The origin of the Chern invariant is the fact that for a loop C on a closed surface, the *inside* of C used in equation 3.8 is arbitrary, so that the surface integral over the inside and the outside must agree with one another up to a multiple of 2π . It follows that the Berry curvature integrated over the entire surface must be $2\pi n$ [4].

The change of the topological invariant number induces gapless conducting states at the interface between topological trivial and non-trivial phases. In the integer quantum Hall state this leads to chiral edge states at the interface of vacuum (topological trivial insulator, $n = 0$) and the quantum Hall state ($n = 1$). In a semiclassical picture these edge states arise from skipping orbits that electrons undergo as their cyclotron orbits bounce off the edge (see figure 3.4). They are called chiral because they only propagate in one direction only along the edge. These states are insensitive to disorder because there are no states available for backscattering [4].

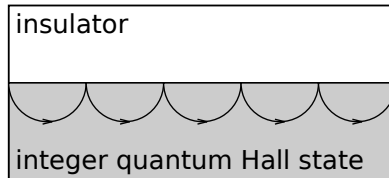


Figure 3.4: Chiral edge states at the interface between vacuum and the integer quantum Hall state. Electrons describe a skipping cyclotron motion at the edges. Figure taken from [12].

3.2 Graphene

Another prominent example of the quantum Hall state is graphene. The Dirac electrons present in graphene show strong parallels to the surface of a topological insulator. D. Haldane invented a toy-model based on graphene that shows that the quantum Hall effect can occur without the need for a strong magnetic field or Landau levels and instead

3 Topological insulator

only requires a standard Bloch band structure with broken time-reversal symmetry \mathbb{Z} . This model was later called quantum anomalous Hall effect and is the predecessor to the time-reversal invariant topological insulator [10].

Graphene is a single layer of carbon atoms arranged in a honeycomb lattice (see figure 3.5 (a)). At two distinct points, namely K and K' , in the Brillouin zone valence and conduction band touch each other. Near those points the electronic dispersion resembles the linear dispersion of massless relativistic particles, described by the Dirac equation. Due to the two sublattices in graphene the Hamiltonian can be written in a 2×2 matrix [1],

$$H_0(\vec{k}) = \begin{pmatrix} 0 & h(\vec{k}) \\ h^\dagger(\vec{k}) & 0 \end{pmatrix}, \quad (3.14)$$

with \vec{k} in the x-y plane and $h(\vec{k}) = t_1 \sum_i \exp(i\vec{k} \cdot \vec{a}_i)$. Nearest neighbor hopping is described by t_1 and \vec{a}_i are the three vectors connecting a site to its nearest neighbors. With the use of Pauli matrices $\vec{\sigma}$, the Hamiltonian can be simplified to

$$H_0(\vec{k}) = t_1 \sum_i [\sigma_x \cos(\vec{k} \cdot \vec{a}_i) - \sigma_y \sin(\vec{k} \cdot \vec{a}_i)]. \quad (3.15)$$

The gapless Dirac points are topologically protected but only if both inversion symmetry \mathcal{P} and time-reversal symmetry \mathbb{Z} are present. Inversion symmetry \mathcal{P} exchanges the site A with the site B . The time-reversal operator takes the complex conjugate of a wave function, reverses momentum $\vec{k} \rightarrow -\vec{k}$ and flips the spin. In the Haldane model the electrons are considered to be fully spin-polarized, which means that spins are neglected. Thus without spin the time-reversal symmetry operator \mathbb{Z} is just the complex conjugation,

$$H_0(\vec{k}) = H_0^*(-\vec{k}). \quad (3.16)$$

Haldane wanted to open the gap at the Dirac points by breaking either the inversion (sublattice) \mathcal{P} or time-reversal symmetry \mathbb{Z} . One way to break inversion symmetry \mathcal{P} is to assign different masses for site A and B . The semiconductor boron nitride (BN) for example also crystallizes in a honeycomb structure but with two different elements at the two sites in the unit cell [10]. The result of breaking inversion symmetry in boron nitride is a band gap. The Hamiltonian for opposite onsite energy M or $-M$ is

$$H(\vec{k}) = H_0(\vec{k}) + M\sigma_z \quad (3.17)$$

This leads to a gapped band structure,

$$E(\vec{k}) = \pm \sqrt{(|h(\vec{k})|^2 + M^2)}. \quad (3.18)$$

Taking the limit $|M| \gg t_1$ shows that the electronic states will only be localized in

3.2 Graphene

one of the two sublattices A or B . This case of breaking the inversion symmetry \mathcal{P} is topologically trivial and has no edge states [1].

Haldane introduced breaking time-reversal symmetry in graphene by adding complex second-nearest neighbor hopping constants to the Hamiltonian. This can be done by applying a staggered magnetic field that is zero on the average, but has all of the spatial symmetries of the honeycomb lattice. Second neighbor hoppings can either be clockwise or anticlockwise, where clockwise rotation is expressed by the complex amplitude t_2 and anticlockwise is expressed by t_2^* . Time-reversal symmetry is now broken because hopping to the second nearest neighbor clockwise does not have the same amplitude than hopping counterclockwise. When the gap opens at the Dirac points, the Dirac equation is no longer massless and the Hamiltonian with broken time-reversal symmetry reads [1],

$$H(\vec{k}) = H_0(\vec{k}) + M\sigma_z + 2t_2 \sum_i \sigma_z \sin(\vec{k} \cdot \vec{b}_i). \quad (3.19)$$

The last term in equation 3.19 is called *mass term*. The *mass term* decides whether the masses at K and K' are same signs, $m = m'$ or opposite signs, $m = -m'$. Haldane showed that for opposite signs of the masses at K and K' the gapped state is not an insulator but rather a quantum Hall state with $\sigma_{xy} = e/h$.

This can be visualized by looking at the zigzag edge of graphene (see figure 3.5 (c)) when the gap opens. The zigzag edge states of graphene are zero modes because particle-hole symmetry in the *bulk* requires an equal number of B sites and A sites. Any excess of one type of site over the other appears as zero energy mode (see figure 3.5 (b)). The edge states connect the projections of the bulk Dirac points [10].

When the gap opens by second neighbor hopping, the edge state has to remain attached to the valence and the conduction band at each of the two projections of the Dirac points (see figure 3.5 (d)). In the case of broken inversion symmetry \mathcal{P} the edge state is either only connected to the valence or the conduction band, resulting in a trivial insulator. In the case of broken time-reversal symmetry \mathbb{Z} however the edge state becomes a conduit by connecting valence and conduction band. This is a fundamental property of the bulk-boundary correspondence. Charge is not conserved at edge states and thus electrons can appear at the edge seemingly out of nowhere, when in reality they are being depleted from the other edge and pumped through the bulk until they appear at the edge [1]. But for this to happen a conduit connecting valence and conduction band has to be present in the quantum Hall state [10].

The edge state in figure 3.5 (d) can be attributed with a positive (negative) group velocity $(\pm)\hbar v_F$ if the slope connecting valence and conduction band is positive and vice versa. By changing the Hamiltonian near the surface, the edge state could develop a kink, intersecting the Fermi energy three times (see figure 3.6) and resulting in three different edge modes. The difference between right moving N_R and left moving modes N_L however stays the same [12],

$$N_R - N_L = \Delta n, \quad (3.20)$$

3 Topological insulator

where Δn is the Chern number across the interface. This property of the edge states is determined by the topological structure of the bulk states and is a consequence of the bulk-boundary correspondence.

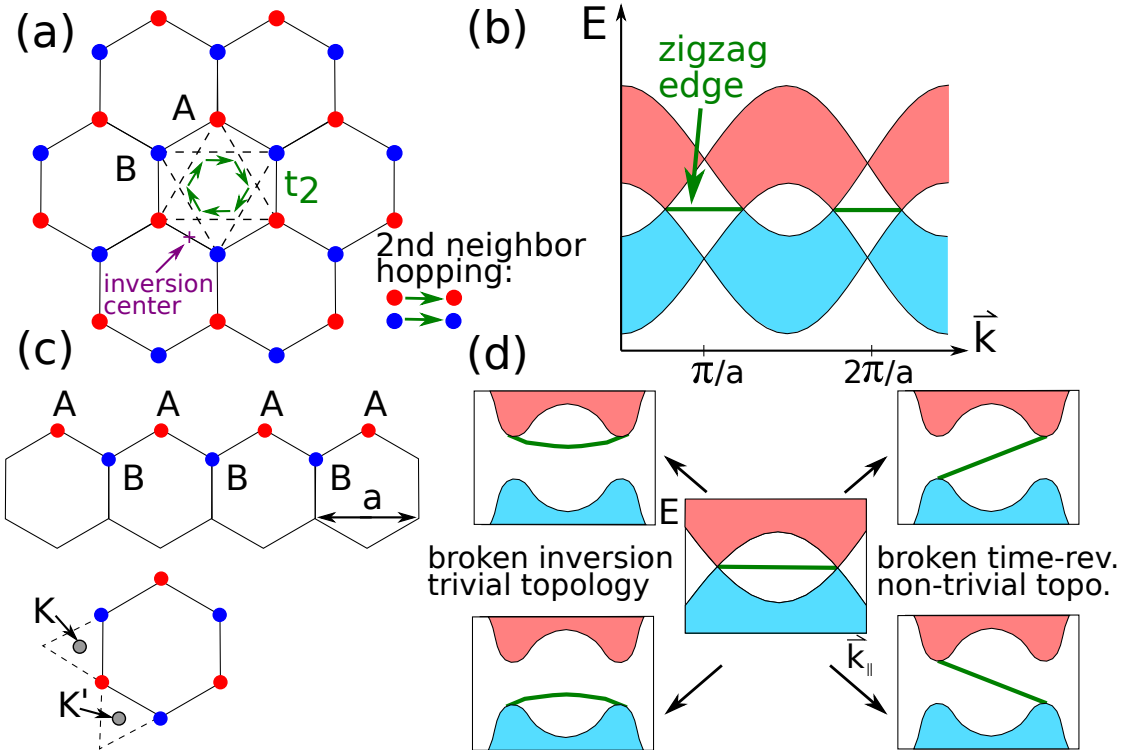


Figure 3.5: (a) Honeycomb lattice of graphene shows the sites *A* and *B*. The green arrows indicate second neighbor hopping from site *A* to *A* or from site *B* to *B*. (b) Band structure for a zigzag edge of graphene. Zero energy mode (green) connects the projections of the Dirac points when the energy gap is closed. The blue and red area show the bulk of graphene. (c) Zigzag edge of graphene with an excess of *A* sites over *B* sites which leads to zero energy edge states in graphene because of particle-hole symmetry. (d) The four different ways for the zigzag edge state to connect the valence or conduction band. The left hand side shows the trivial topology of an ordinary insulator, when the zigzag edge state connects both to the valence band or conduction band. Whereas the right hand side depicts the edge state, that connects valence to conduction band. Figure adapted from [1] [10].

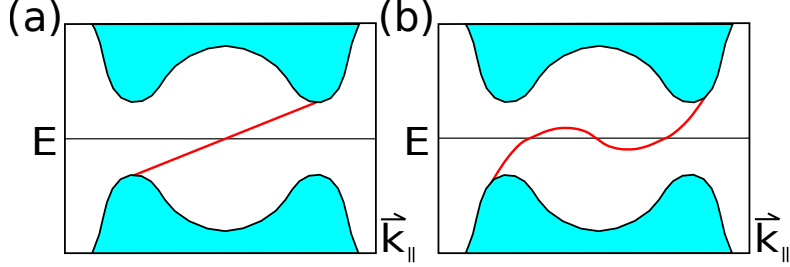


Figure 3.6: Edge states in graphene for different Hamiltonians. Both have an edge state, that connects valence to conduction band. They only differ in the number of times the edge state crosses the Fermi energy. The difference between right moving and left moving modes in (b) is a topological invariant. Figure taken from [4]

3.3 Quantum spin Hall state

In the previous chapter a quantum Hall state in graphene was achieved by conserving inversion symmetry \mathcal{P} and breaking time-reversal symmetry \mathbb{Z} . This was done by applying a staggered magnetic field. C. Kane and E. Mele invented a model for graphene that shows, that edge states exist and are protected by time-reversal symmetry \mathbb{Z} without the need of an external magnetic field. In the Haldane model the spin of the electrons was neglected. In the Kane-Mele model the spin-orbit interaction is used to define a spin dependent second neighbor hopping term. Since time-reversal symmetry \mathbb{Z} flips both the spin and σ_{xy} , the Hamiltonian of the system decouples into two independent Hamiltonians for the up and down spins [12],

$$H = \begin{pmatrix} H_\uparrow & 0 \\ 0 & H_\downarrow \end{pmatrix}. \quad (3.21)$$

This effectively leads to two copies of the integer quantum Hall state (Haldane model) with different spins. Applying an electric field \vec{E} results in up and down spins moving in opposite directions (see figure 3.7 (a)). The Hall conductivity is zero, but there is a total net flow of spin. Since the Kane-Mele model is basically two copies of the Haldane model, two edge states, where up and down spins propagate in different directions along the edge, must exist. These edge states, called helical edge states, are degenerate at $\vec{k} = 0$. Degeneracy can usually be lifted by arbitrary weak perturbations, for example perturbations violating the conservation of spin. However C. Kane showed the degeneracy at $\vec{k} = 0$ could not easily be lifted. He showed that the reason for this behavior of the edge states is the so called Kramers theorem. Kramers theorem states that for spin 1/2 electrons the time-reversal operator \mathbb{Z} has the property $\mathbb{Z}^2 = -1$. It follows that all eigenstates of a time-reversal invariant Hamiltonian are at least twofold degenerate. Thus the edge states at $\vec{k} = 0$ build a Kramers pair and cannot be lifted by any time-reversal invariant perturbation, even if the conservation of spin is violated [12].

3 Topological insulator

As already mentioned the time-reversal operator \mathbb{Z} flips the spin and takes the complex conjugate of a wavefunction. For a time-reversal invariant system $\mathbb{Z}|\psi\rangle$ and $|\psi\rangle$ have the same energy. If it can be proven that $\mathbb{Z}|\psi\rangle$ and $|\psi\rangle$ are two different eigenstates (for $\mathbb{Z}^2 = -1$), it proves that Kramers theorem is correct. The plan is to assume that $\mathbb{Z}|\psi\rangle$ and $|\psi\rangle$ give the same quantum state and then proving that this leads to a contradiction [24].

$$\mathbb{Z} |\psi\rangle = \exp^{i\phi} |\psi\rangle \quad (3.22)$$

(same quantum state with only a phase difference)

$$\mathbb{Z}^2 |\psi\rangle = \mathbb{Z} \exp^{i\phi} |\psi\rangle = \exp^{-i\phi} \mathbb{Z} |\psi\rangle = \exp^{-i\phi} \exp^{i\phi} |\psi\rangle = |\psi\rangle$$

$$\mathbb{Z}^2 |\psi\rangle = +1 |\psi\rangle$$

But this violates the assumption that $\mathbb{Z}^2 = -1$. This proves Kramers degeneracy of spin 1/2 particles under time-reversal symmetry.

C. Kane also showed that even strong disorder, for example a lot of dirt on the sample, would not cause a lifting of the degeneracy at $\vec{k} = 0$. Dirt on the edge of the sample can be viewed as a typical scattering problem along the edge. Imagining the edge disordered for a finite length but clean on both ends of the disordered region, C. Kane showed that the reflexion amplitude is odd under time-reversal symmetry \mathbb{Z} , thus causing the incident electron to be completely transmitted through the disordered region and the reflexion amplitude to be zero. Thus the helical edge states at $\vec{k} = 0$ are robust against spin non-conserving perturbations and strong disorder [12].

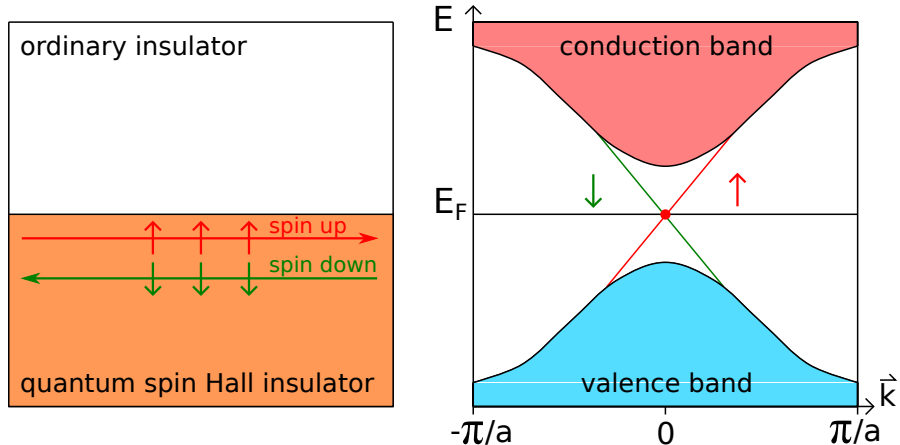


Figure 3.7: (a) The spins of boundary states propagate with opposite group velocities along the edge in a quantum spin Hall insulator. (b) Band structure of the edge states of graphene in the first Brillouin zone. Degeneracy at $\vec{k} = 0$ is protected by time-reversal symmetry \mathbb{Z} . Figure taken from [12].

3.4 Z_2 topological insulator

In general, Kramers theorem states that under time-reversal symmetry for any Bloch eigenstate $|\psi\rangle$ there is another eigenstate $\mathbb{Z}|\psi\rangle$ with the same energy. These Kramers doublets are located at different momentum points \vec{k} and $-\vec{k}$. For a crystal states in the Brillouin zone with the momentum $\Gamma_a = 0$ and $\Gamma_b = \pi/a$ are degenerate because under time-reversal symmetry $\vec{k} \rightarrow -\vec{k}$ and \vec{k} is the same as $-\vec{k}$ at 0 and π/a (edge of the Brillouin zone). For any momentum except $\vec{k} = \Gamma_{a,b}$ spin-orbit coupling lifts the degeneracy. Depending on the Hamiltonian near the edge there may or may not be edge states inside the energy gap. If there are edge states, then these states at Γ_a and Γ_b have to be connected because energy is a smooth function of \vec{k} . There are two different possibilities to do this. First the two states at $\Gamma_a = 0$ connect both to the Kramers doublet at $\Gamma_b = \pi/a$ (as seen in figure 3.8 (a)). Another way is to connect the two states at $\Gamma_a = 0$ to two different Kramers doublets at $\Gamma_b = \pi/a$, resulting in a zigzag shape of the edge states (3.8 (b)) [12].

For the first case (3.8 (a)) there is always an even number of edge states (e.g. zero, two, four pairs) and they can be eliminated by pushing all of the bound states out of the energy gap (similar to chapter 3.1 with $H(\alpha)$). In the second case an odd number of edge states exists. There are always an odd number of left moving edge states and the same number of right moving edge states, that cannot be pushed out of the energy gap. The first case indicates a trivial insulator, whereas the second case describes a non-trivial insulator. Since time-reversal symmetry only allows two kinds of insulators, they are labeled Z_2 topological insulators [24].

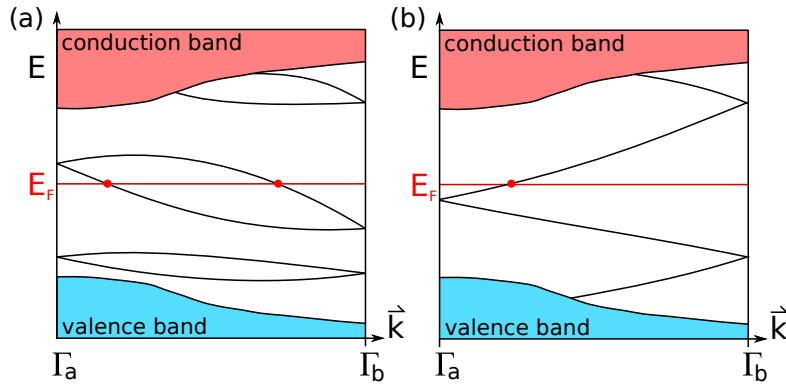


Figure 3.8: Band structure of two boundary Kramers degenerate points $\Gamma_a = 0$ and $\Gamma_b = \pi/a$. The Brillouin zone $-\pi/a < \vec{k} < 0$ is not shown because \mathbb{Z} requires $-\pi/a < \vec{k} < 0$ and $0 < \vec{k} < \pi/a$ to be mirror images of each other. Connecting the Kramers doublets at Γ_a and Γ_b leads to (a) an even number of Kramers doublets or (b) an odd number of Kramers doublets crossing the Fermi energy. Only (b) has topologically protected metallic boundary states. Figure taken from [12].

3.5 3D topological insulator

Topological insulators stabilized by time-reversal symmetry can be generalized to 3D. 3D topological insulators are described by four Z_2 topological indices. Three of them are known as weak topological indices and the last one is known as the strong topological index. Considering the 3D Brillouin zone of a 3D insulator, planes with constant k_z can each be viewed as a 2D system. Most of those planes are not time-reversal invariant because \mathbb{Z} causes $k_z \rightarrow -k_z$. However the planes at $k_z = -\pi/a$, $k_z = 0$ and $k_z = \pi/a$ are time-reversal invariant because k_z is the same as $-k_z$ at points π/a and 0 (see figure 3.9). The planes $k_z = 0$ and $k_z = \pi/a$ are 2D time-reversal invariant insulators. The question is whether these two planes are topological insulators or trivial insulators. There are three possibilities: both trivial, both topological, one topological and one trivial. If both are trivial, then the 3D insulator is also topologically trivial. If both are nontrivial, then the 3D insulator is a weak topological insulator. But if one is trivial and the other is topological, then the 3D insulator is a strong topological insulator [24] [12].

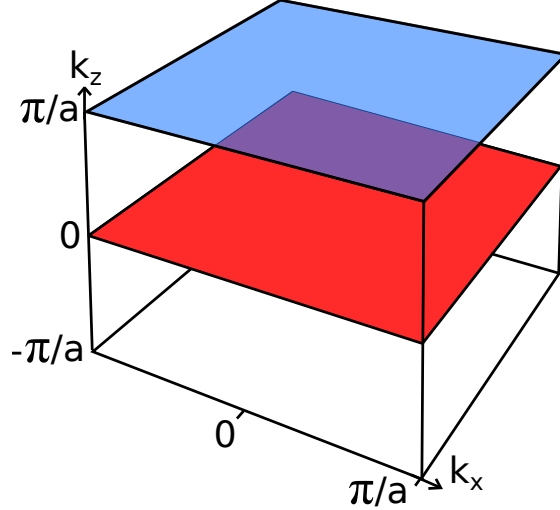


Figure 3.9: Three planes at $k_z = -\pi/a$, $k_z = 0$ and $k_z = \pi/a$, which are time-reversal protected because k_z is the same as $-k_z$ at points π/a and 0. Figure taken from [24].

3.5.1 Weak topological insulator

In a weak topological insulator, both planes $k_z = 0$ and $k_z = \pi/a$ have edge states. Each plane has one pair of edge states. The red dots in figure 3.10 (a) denote the Fermi surface for the edge states. The Fermi surface has to be a closed loop, which cannot have starting or end points. Thus by connecting the six points of Fermi surfaces a

result similar to figure 3.10 (b) is obtained. This figure illustrates that for a 3D weak topological insulator, the 2D surface is a metal and this surface metal has open Fermi surfaces. Therefore the weak 3D topological insulator is just a stack of 2D topological insulators. The same process can be repeated for k_x and k_y [12].

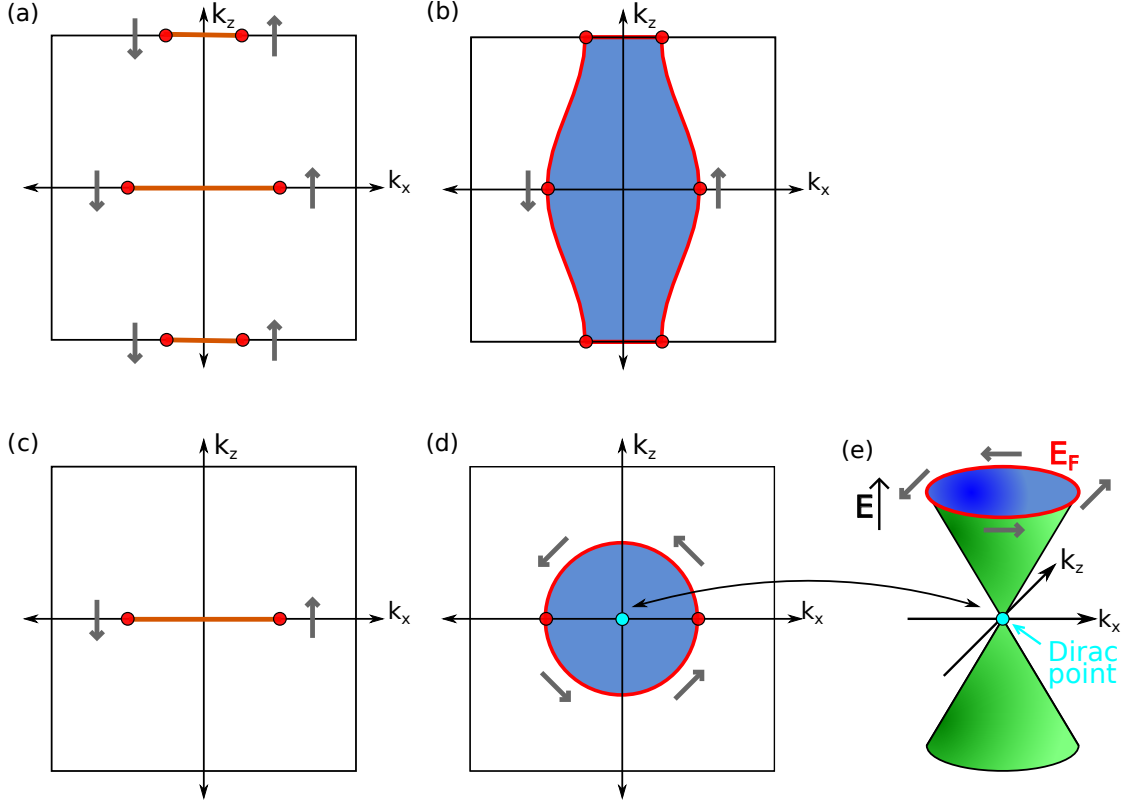


Figure 3.10: (a) Side view of three time-reversal invariant planes, where each plane has a pair of edge states. Red points denote the Fermi surface. (b) Closing the Fermi surface, the surface metal has open Fermi surfaces. (c) Side view of three time-reversal invariant planes, where only one has a pair of edge states. (d) Closing the Fermi surface, the surface metal has a closed Fermi surfaces. (e) In a strong topological insulator the Fermi surface encloses a single Dirac point. Figure taken from [12].

3.5.2 Strong topological insulator

For a strong topological insulator, only one of the planes at $k_z = 0$ has edge states. Again the dots in figure 3.10 (c) indicate the Fermi surface for the edge states, which cannot have starting or end points. Connecting the two points of Fermi surfaces results in a circle in the k_{xz} plane (Fig. 3.10 (d)). For a 3D topological insulator the 2D surface is a

3 Topological insulator

metal and this surface metal has a closed Fermi surface with unique properties. Unlike an ordinary metal, which has up and down spins at every point on the Fermi surface, the surface states of the strong topological insulator are not spin degenerate [12]. Time-reversal symmetry \mathbb{Z} requires that states with opposite \vec{k} have opposite spins, which is indicated in figure 3.10 (e). If an electron moves around the Fermi circle, it acquires a nontrivial Berry phase π . This Berry phase results in weak antilocalization when increasing the temperature in the presence of disorder. Whereas an ordinary 2D electron gas would show weak localization due to Anderson localization [4].

The three first materials that were confirmed to be 3D topological insulators were $\text{Bi}_x\text{Sb}_{1-x}$, Bi_2Se_3 and Bi_2Te_3 . ARPES (angle-resolved photoemission spectroscopy) can be used to probe the surface states of a topological insulator. In an ARPES experiment the sample is illuminated by photons and the energy and angle, at which the photoelectrons are emitted, are measured. Light with energy close to the Fermi energy of the sample is used to probe the surface states and reconstruct the band structure. Figure 3.11 shows an ARPES measurement of Bi_2Se_3 taken by J. Moore.

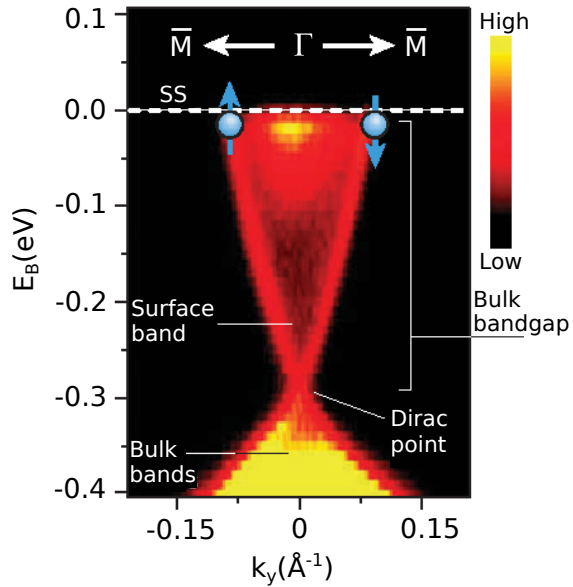


Figure 3.11: An ARPES measurement of Bi_2Se_3 shows the bandstructure of a metallic-like surface state. The electron energy E_B is plotted against the momentum k_y and a high density of states is indicated by a yellow or red color. The surface bands are crossing the band gap at a single Dirac point. The spin of the surface states is shown by blue arrows. Figure taken from [17].

3.6 Charge to spin conversion

In a strong topological insulator spins with opposite sign propagate in different directions due to time-reversal symmetry. Since the spin of the surface states is locked at a right angle to their momentum (spin-momentum locking) a conversion between spin and momentum is possible. As described in chapter 2.5, in a topological insulator/ferromagnet heterostructure the precessing magnetic moments \vec{m} in the ferromagnet layer can pump spin into the non-magnetic topological insulator layer in FMR. If the non-magnetic layer is chosen to be a strong topological insulator, like BiSbTeSe (BSTS), then the spin current pumped into the topological insulator layer can be converted to a charge current through spin-momentum locking [12]. In principle this conversion can occur at a perfect rate $q_{\text{ICS}} = J_s/j_c$, where J_s is the spin current in the ferromagnet and j_c is the charge current on the surface of the topological insulator.

4 Experimental setup and processing of data

This chapter covers the experimental setup and the methods used to evaluate the recorded data. In the first part the setup of the experiment for measuring the ferromagnetic resonance will be described and every important component and its function will be explained. Then the evaluation of a typical recorded measurement curve will be showcased for a FMR resonance curve. Afterwards the fit model for measuring the voltages along the sample stripe is also discussed.

4.1 Experimental setup

The central element of the experimental setup is the cryostat, which is used to measure the temperature dependence of ferromagnetic resonance. FMR can be measured by exciting the magnetic moments in the sample by a microwave field \vec{h} in a constant external magnetic field \vec{H}_0 . The magnetic moments will start to precess around the effective field. The microwave field will be supplied by a coplanar waveguide, on top of which the sample will be mounted. If the microwave frequency is constant and the external magnetic field is changed, the absorption of the microwaves in the sample will be at a maximum when \vec{H}_0 reaches \vec{H}_{FMR} .

The cryostat used in the setup works like a Gifford-McMahon-Cryocooler. A compressor ejects compressed helium into the cryostat. The helium then expands and therefore cools the sample, which is located inside the cryostat beneath two cooling shields. The temperature can be controlled by a heater and a PID temperature controller is used to keep temperature constant. For thermal isolation a vacuum is generated inside the cryostat first by a backing pump and then a turbo molecular pump. Temperatures from room temperature to approximately 10 Kelvin can be reached. A microwave generator can produce microwaves with frequency from 2 to 30 GHz and vary its power from 10 dB to 20 dB. A coaxial cable connects the microwave generator to the sample mounted at the cold head of the cryostat. The sample holder connects to a coplanar waveguide, in whose magnetic field the sample is located. The sample absorbs some of the microwaves and the rest is transmitted to a Schottky diode outside of the cryostat, where a voltmeter measures the voltage along the sample stripe. The voltage on the

4.1 Experimental setup

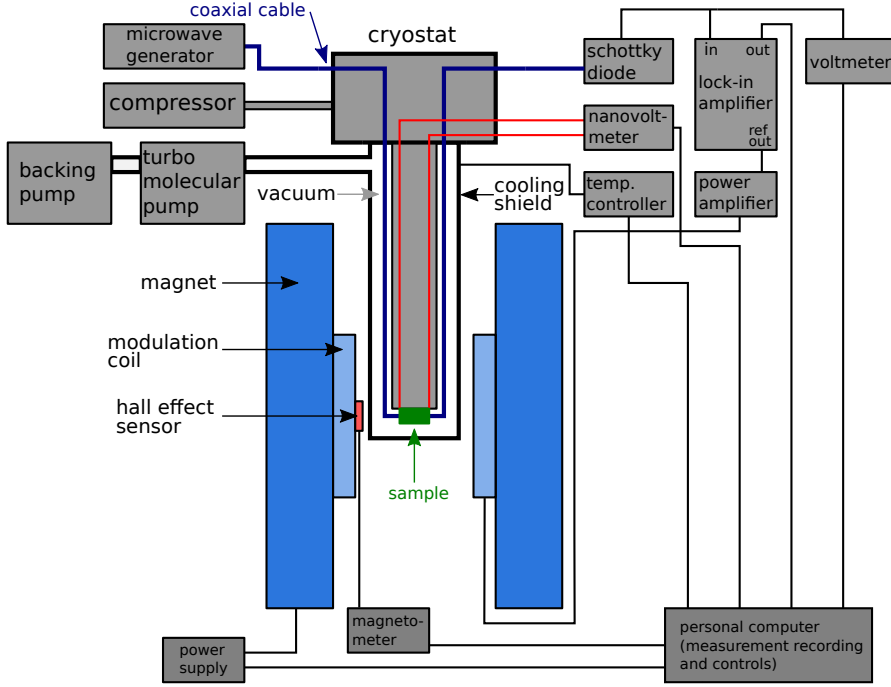


Figure 4.1: In this illustration the experimental setup is shown. The microwave generator generates microwaves, that are transmitted through a coaxial cable to the sample located in the middle of the pole pieces of the electromagnet. The intensity of the microwaves is changed due to the absorption of energy by the precessing magnetization. The transmitted microwave power is measured by a Schottky diode. In order to perform a FMR measurement the external magnetic field \vec{H}_0 is slowly increased, whereas the microwave frequency stays constant. A lock-in amplifier is used to reduce noise in the measurements and a nanovoltmeter records the voltage, produced by spin pumping, along the sample stripe. Figure taken from [16]

Schottky diode is a measure for the transmitted microwave power.

The external magnetic field \vec{H}_0 is created by an electromagnet with the cryostat mounted between its pole pieces. In the middle of those pole pieces, where the magnetic field is nearly constant the sample is located. For measuring the magnetic field of the coils a Hall probe is used. The sensor is located outside of the cryostat and therefore has to be calibrated accordingly to read the magnetic field inside the cryostat at the sample position. A Gauss meter measures the magnetic field and transmits the data to a PC. The microwave power changes after it passes the sample because the sample absorbs some of the energy of the microwaves. A lock-in amplifier is utilized to measure the marginal change of the microwave transmission during FMR. The lock-in modulates the signal from the Schottky diode by a sinusoid shaped reference signal at 86 Hz. The frequency 86 Hz is used because it is not a multiple of the power line frequency at 50

4 Experimental setup and processing of data

Hz and therefore reducing the noise due to nearby electric devices. The reference signal is amplified and drives the modulation coils creating a small magnetic modulation field at the sample position. The lock-in extracts the signal with the same frequency as the reference frequency and a preset phase correlation. This process significantly reduces noise in the measurements.

In order to make assumptions about spin pumping in the sample, the sample stripe is contacted on both ends and the voltage is measured by a nanovoltmeter outside of the cryostat, which is connected to a computer.

4.2 Coplanar waveguide

A coplanar waveguide (CPW) consists of three parallel conducting tracks. The middle conducting line is called the signal line and is used to guide signals in the microwave frequency range. On either side of the signal line separated by a small gap, two ground lines return the signal from the signal line. All three conducting lines are fabricated onto the same side of a dielectric substrate and are therefore called *coplanar*. The sample can be placed onto the CPW in two different configurations. In the in-plane configuration the probe stripe is on top and parallel to the signal line. The microwave magnetic field \vec{h}_i is parallel to the surface of the sample. The signal line and hence also the direction of the sample stripe are chosen to be in Y-direction in the XYZ coordinate system from chapter 2.4.2.1. The in-plane microwave excitation magnetic field \vec{h}_i is pointed in the X-direction and can be expressed as

$$\vec{h}_i = \begin{pmatrix} \cos(\varphi_M)h_i \\ \sin(\varphi_M)h_i \\ 0 \end{pmatrix} \quad (4.1)$$

in the xyz coordinate system. At $\varphi_M = 0^\circ$ the y-component of \vec{h}_i is zero and no excitation of the magnetic moments in the sample are possible because $h_i \parallel \vec{M}$. According to chapter 2.6.1 V_{AMR} is proportional to $\sin(2\varphi_H)$ [2]. The AMR voltage disappears at $\varphi_H = 0^\circ$ and all multiples of 90° . The voltage generated by a topological insulator V_{TI} however is given by a $\cos(\varphi_H)$ dependence [2]. V_{TI} is zero at $\varphi_H = 90^\circ$ and is maximal at $\varphi_H = 0^\circ$. Therefore V_{TI} can be separated from V_{AMR} at an angle $\varphi_H = 0^\circ$ [9] but as mentioned before at $\varphi_H = 0^\circ$ there can be no excitation achieved in in-plane configuration. This problem can be solved by putting the sample stripe in between the signal and the ground line of the CPW. The excitation magnetic field \vec{h}_o is now perpendicular to the XY-plane and at $\varphi_M = 0^\circ$ excitation can be achieved. This is called the out-of-plane configuration and is illustrated in 4.2. In the out-of-plane configuration there will always be excitation regardless of the angle φ_M as long as the external magnetic field \vec{H}_0 lies in the XY-plane. However the out-of-plane configuration has the drawback of a smaller excitation magnetic field because of the larger distance between sample and

signal line. In the out-of-plane configuration V_{TI} can be separated from V_{AMR} at an angle $\varphi_H = 0^\circ$.

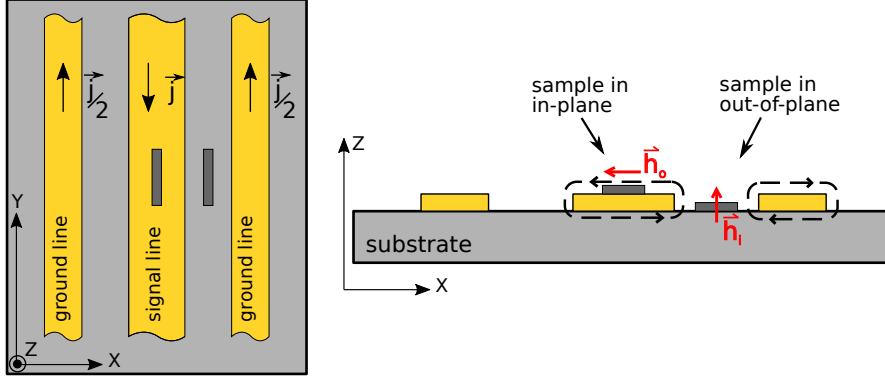


Figure 4.2: The structure of a coplanar waveguide (CPW) is shown from the top and side. Three conducting tracks are fabricated on top of a substrate, where the track in the middle (signal line) carries the microwave signal and the other tracks are the grounded return conductors. In the in-plane configuration the sample is located on top of the signal line with the microwave excitation field in the XY-plane. In the case of the out-of-plane configuration the sample is located in between the signal line and a ground line. With the external magnetic field \vec{H}_0 lying in the XY-plane, the out-of-plane configuration always results in an excitation of the magnetic moments in the sample. Figure taken from [7].

4.3 Lithography

The sample examined in this thesis consists of two halves with different layers. On one half of the sample consists of a layer of permalloy (Py) on the bottom of a layer of a topological insulator BiSbTeSe (BSTS). On the second half a layer of copper is separating the Py and the BSTS. The illustration 4.3 shows the general structure of the sample. The sample stripe is fabricated in out-of-plane configuration, as mentioned in the previous chapter, in between the signal and the ground line on top of the Al_2O_3 substrate. Both ends of the sample stripe are connected with gold contacts and the voltage along the stripe can be measured. Those gold pads can be bonded to a sample holder with aluminium wires and then be mounted into the cryostat, as can be seen in the illustration 4.1. The sample holder is connected to the microwave generator and the nanovoltmeter through a coaxial cable. The CPW is also made up of gold and is isolated from the sample by an aluminium oxide layer Al_2O_3 .

The sample is produced by firstly cutting an Al_2O_3 waver into $5 \text{ mm} \times 5 \text{ mm}$ pieces. After cleaning the pieces in a ultrasonic cleaner optical lithography is used. For this purpose

4 Experimental setup and processing of data

a photoresist layer is put on top of the Al_2O_3 waver. The waver with the photoresist is then exposed to light through a mask of the desired shape of the sample stripe in between the light source and the waver. A developer will dissolve the photoresist, which was not covered by the mask (positive lithography) and leave behind a coating of the inversed pattern of the sample shape. After etching the exposed pattern, the final step is the lift-off, where the photoresist is washed out, leaving behind the desired shape of the Py/BSTS-double layer. Next the stripe has to be contacted by gold. Here optical lithography was used again in the same manner. Then a layer of aluminium oxide is deposited on top of the stripe, where the gold contact pads at the end of the stripe remain uncovered. Finally the structure of the CPW was grown on the sample with gold also using optical lithography.

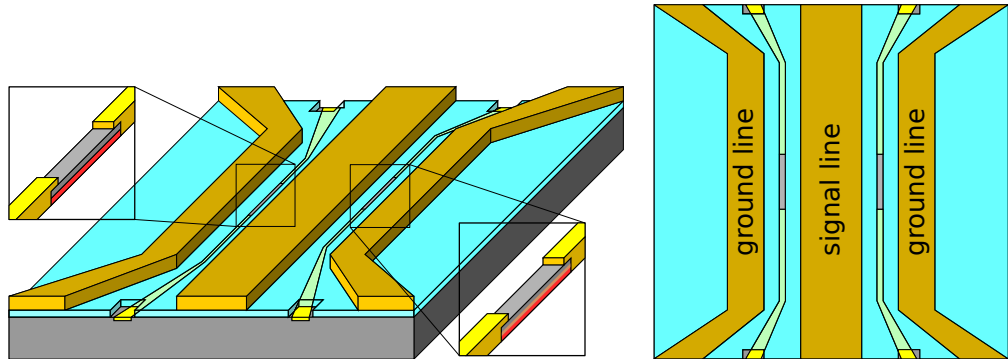


Figure 4.3: A CPW is shown with two sample stripes in the out-of-plane configuration.

The sample stripes each consist of a bottom layer permalloy (red) and a top layer of BSTS, where one of the sample stripes also has a third copper layer in between the BSTS and the permalloy layers. The stripes are structured onto a Al_2O_3 substrate. Optical lithography was used to fabricate the sample stripes. Gold contacts (yellow) connect to both ends of the sample stripes and lead to the edges of the substrate. An isolating layer of Al_2O_3 separates the sample stripes from the CPW grown on top of the sample stripes.

4.4 Processing the data

4.4.1 Evaluation and fit of resonance curve in FMR

In an FMR-experiment the external magnetic field H_0 is increased continually at a constant microwave frequency ω . The microwave absorption of the sample is, after rectification using a Schottky diode, measured with a lock-in amplifier and recorded by a computer, where the spectra have to be processed before they can be evaluated. The absorption of microwaves by the sample is proportional to the imaginary part of χ_{zz} ,

4.4 Processing the data

which has the form of a symmetric Lorentian line shape [5] [28]. The total absorption however is proportional to an asymmetric Lorentzian line shape, since a dispersive component is also present, whose line shape is proportional to the real part of χ_{zz} . As explained in chapter 4.1, using the lock-in technique the measured signal is modulated by a reference frequency in order to reduce the noise. The lock-in amplifier is therefore only sensitive to the change of the absorbed microwave power with respect to the magnetic field. Thus the actually measured line shape by the computer is the derivative $d\chi_{zz}/dH_0$ of the FMR resonance curve. The fit function $f(H_0)$ reads therefore [16],

$$f(H_0) = \frac{d}{dH_0} \left(\text{Im}(\chi_{yy}) \cos \epsilon + \text{Re}(\chi_{yy}) \sin \epsilon \right) \quad (4.2)$$

$$= A \left(-\frac{2\Delta H^3(H_0 - H_{\text{FMR}}) \cos \epsilon}{((H_0 - H_{\text{FMR}})^2 + \Delta H^2)^2} + \frac{\Delta^2(\Delta H^2 - (H_0 - H_{\text{FMR}})^2) \sin \epsilon}{((H_0 - H_{\text{FMR}})^2 + \Delta H^2)^2} \right), \quad (4.3)$$

where A is the FMR amplitude. In real measurements in addition to equation 4.2 an offset and a slope have to included to the fit. With this fit function the resonance magnetic field H_{FMR} and the line width ΔH can be determined. Furthermore the line width ΔH changes with frequency [28]

$$\Delta H = \Delta H(0) + \frac{\alpha\omega}{\gamma}, \quad (4.4)$$

where $\frac{\alpha\omega}{\gamma}$ is a result of intrinsic mechanisms in the sample, e.g. eddy currents, direct magnon-phonon scattering or relaxation by itinerant electrons. Whereas extrinsic mechanisms, e.g. defects or inhomogeneity in the sample, cause an offset $\Delta H(0)$. By plotting ΔH in respect to the microwave frequency ω the Gilbert damping parameter α can be obtained by taking the derivative of the frequency dependence of the line width.

For almost purely antisymmetric FMR measurement curves the resonance magnetic field H_{FMR} and the line width ΔH can be directly read off the line shape. The line width is proportional to the distance ΔH^{PP} between the maxima and minima of measured curve (see figure 4.4) [16],

$$\Delta H = \sqrt{3}/2\Delta H^{\text{PP}} \quad (4.5)$$

4.4.2 Evaluation and fit of voltages

In chapter 2.6 the voltages present in a permalloy/topological insulator heterostructure were discussed. The voltage signal due to AMR has both a symmetric and antisymmetric

4 Experimental setup and processing of data

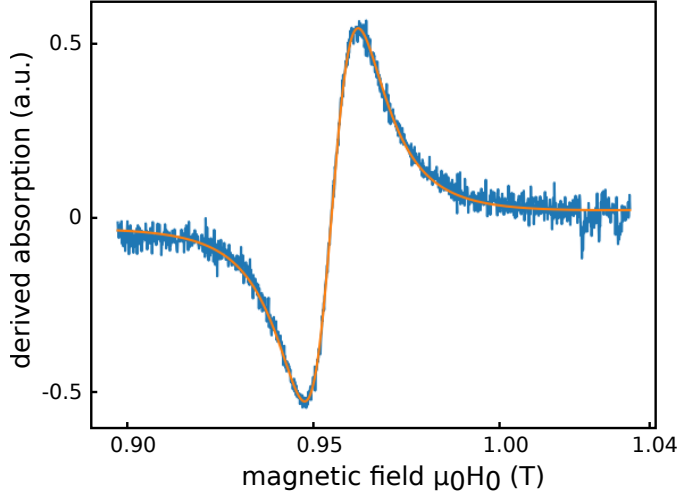


Figure 4.4: Typical FMR measurement (blue) with the fit function 4.2 (orange). The fit parameters yield the line width $\mu_0 \Delta H = 12.4$ mT and the resonance magnetic field $\mu_0 H_{\text{FMR}} = 955$ mT at 39 GHz.

Lorentzian line shape, whereas the voltage caused by spin-momentum locking in the surface states of the TI has a purely symmetric Lorentzian line shape. Thus if both voltage contributions in the sample are present the total line shape is expected to be an asymmetric Lorentzian [18] [2].

$$V(H_0) = V_{\text{sym}} \frac{\Delta H^2}{(H_0 - H_{\text{FMR}})^2 + \Delta H^2} + V_{\text{antisym}} \frac{\Delta H(H_0 - H_{\text{FMR}})}{(H_0 - H_{\text{FMR}})^2 + \Delta H^2} + V_{\text{off}} \quad (4.6)$$

The amplitude V_{sym} consists of both the AMR voltage and the voltage in the TI. As discussed in chapter 4.2 at an angle $\varphi_H = 0^\circ$ the AMR voltage contribution disappears and V_{sym} can be used to investigate the voltage caused by the spin-momentum locking in the TI. The antisymmetric amplitude V_{antisym} is purely a measure for the AMR effect. Figure 4.5 shows a typical voltage measurement fitted by equation 4.6. In this thesis experiments were conducted, in which the mixing of both V_{sym} and V_{antisym} was measured in dependence of the angle φ_H and the temperature.

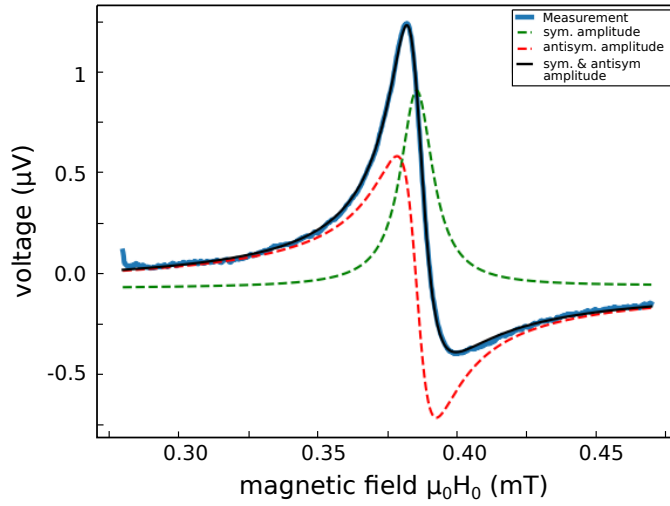


Figure 4.5: Measured voltages on a sample at room temperature at $\varphi_H = 80^\circ$ and a microwave frequency $f = 23$ GHz. The measured voltage (blue) consists of a symmetric part (green) and an antisymmetric part (red). The fit parameters of equation 4.6 yield the symmetric amplitude $V_{\text{sym}} = 0.97$ μV and the anti-symmetric amplitude $V_{\text{antisym}} = -0.130$ μV . The line width $\mu_0 \Delta H = 7.0$ mT and the resonance magnetic field $\mu_0 H_{\text{FMR}} = 385$ mT.

5 Experiments

This chapter inquires the theory of the previous chapters by measurements on a sample consisting of two parts. On one half of the sample a bilayer structure of permalloy Py and topological insulator BSTS is grown and on the other half a trilayer structure of Py, copper Cu and BSTS is grown. On both sides of the $5\text{ mm} \times 5\text{ mm}$ sample a coplanar waveguide structure, as shown in figure 4.3, is patterned. A single coplanar waveguide in the middle of the sample would not suffice since the signal line is too small and the copper layer does not end abruptly, but rather has a gradient with width of about 1 mm at the step edge. The sample was grown by MBE by Matthias Kronseder and the lithography was carried out by Thomas Mayer following the procedures described in chapter 4.3. Chapter 5.1 covers FMR, which is used to obtain the effective magnetization M_{eff} and the damping factor α of the sample. In section 5.2 the dependence of the measured voltage along the stripes on the angle between the external magnetic field and stripe is studied. In chapter 5.3 and 5.4 temperature dependent measurements of the voltage along the stripes were performed at angles $\varphi_H = 45^\circ$ and $\varphi_H = 0^\circ$, respectively, in order to get insight into the behavior of the surface states in the TI at low temperatures. In chapter 5.5 the dependence of the measured voltage along the stripe on the angle between the external magnetic field and the stripe at 10 K is compared to the corresponding room temeperature measurements of chapter 5.2.

5.1 Ferromagnetic Resonance

The FMR measurements shown in this section were not performed in the cryostat FMR setup described in chapter 4.1 (see figure 4.1), but in a different setup used for measurement of fullfilm FMR at room temperature. This setup is used to select a suitable sample for the voltage measurements in the upcoming chapters, since not every sample shows the promise of surface states in the TI. It is called fullfilm FMR since the full $5\text{ mm} \times 5\text{ mm}$ sample can be examined by placing it on the coplanar wave guide without the need for additional lithography steps.

Different substrate materials have been tried out for the growth of the topological insulator/ferromagnet bilayer system, e.g. indium phosphide (InP), strontium titanate (SrTiO_3) or aluminiumoxid (Al_2O_3). Also different materials for the paramagnetic interlayer, e.g. copper (Cu) or silver (Ag), the topological insulator, e.g. bismuth antimony

5.1 Ferromagnetic Resonance

tellurium ($(\text{Bi}_x\text{Sb}_{1-x})_2\text{Te}_3$) and bismuth antimony tellurium selenium BiSbTeSe, and the ferromagnet, e.g. permalloy Py and iron/cobalt alloys $\text{Fe}_x\text{Co}_{1-x}$, have been investigated. In the end the sample T171023-BSTS89 with a Al_2O_3 substrate, 10 nm thick Py layer, 5 nm thick Cu layer and a layer of the topological insulator BiSbTeSe with a thickness of 10 quintuple layers was picked.

This sample shows promising results in the fullfilm FMR measurements. Figure 5.1 depicts the resonance field and the line width plotted against the microwave frequency for these FMR measurements. The FMR resonance curves can be fitted with equation 4.2 to obtain ΔH and H_{FMR} as fit parameters. By using the Kittel equation 2.44, the effective magnetization M_{eff} can be derived by fitting the magnetic resonance field H_{FMR} in dependence of the microwave frequency ω . With the g-factor for permalloy set to 2.10 [19] the effective magnetization for the Py/BSTS side is 0.92 T and for the side with copper 0.62 T. The damping parameter α is acquired by fitting the line width with equation 4.4. For the Py/BSTS side $\alpha = 0.01$ and for the Py/Cu/BSTS side $\alpha = 0.02$. The copper interlayer increases the damping by a factor of two and indicates that the copper is acting as a decoupling layer between the permalloy and the topological insulator. This decoupling is assumed to protect the surface states of the TI, which results in a more efficient transformation from spin current into charge current. Therefore the precession of the magnetic moments \vec{m} in the ferromagnet relaxes faster, which is equivalent to a higher Gilbert damping factor. Another explanation of the results in figure 5.1 is that the copper layer diffused into the permalloy layer and therefore the damping factor increased. The diffusion would explain the reduction of the effective magnetization by the copper interlayer. Another possible explanation for the higher damping factor for Py/Cu/BSTS could be a perpendicular anisotropy of copper K_U^\perp , which would reduce the effective magnetization according to equation 2.22.

5 Experiments

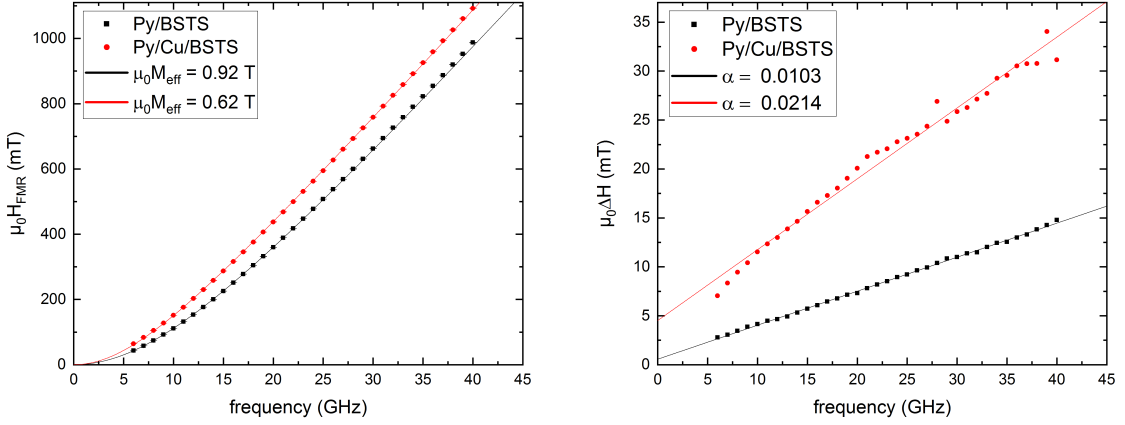


Figure 5.1: Frequency dependence of (a) the resonance magnetic field H_{FMR} and (b) the line width ΔH in the fullfilm sample. By fitting the curve in (a) with the Kittel equation 2.44 the effective magnetizations M_{eff} for Py/BSTS and Py/Cu/BSTS are obtained. (b) By fitting the line width in respect to the microwave frequency with equation 4.4 the Gilbert damping parameter α is obtained. The Py/Cu/BSTS sample shows both a larger effective magnetization M_{eff} and a larger damping parameter α than the Py/BSTS sample.

5.1.1 FMR in the cryostat

The sample is now mounted in the cryostat FMR setup in order to measure the temperature dependence of the TI. However during the lithography process the marker, placed to distinguish the Py/BSTS and Py/Cu/BSTS side, was lost mistakenly. For this reason FMR measurements have been repeated in the cryostat FMR setup to compare the results with the previous chapter and conclude which side is Py/BSTS and which side is Py/Cu/BSTS. A visual distinction can not be accomplished since the sample stripe is only a couple of micrometers broad. Figure 5.2 shows the result of these FMR measurements. Since the sample is now considerably smaller, the signal strength has decreased. Figure 5.2 (a) shows the magnetic resonance field in dependence of the microwave frequency, resulting in an effective magnetization $\mu_0 M_{\text{eff}} = 1.22 \text{ T}$ for the non-copper side and $\mu_0 M_{\text{eff}} = 0.84 \text{ T}$ for the copper side. These values are larger than the values obtained in the fullfilm FMR setup. The effective magnetization on the non-copper side has increased by 0.30 T, whereas the copper side has increased by 0.22 T. The measurements of the damping parameter stay the same approximately. Therefore it is assumed that the measurements marked red in figure 5.2 are from the Py/Cu/BSTS side.

5.2 Angle dependence at room temperature

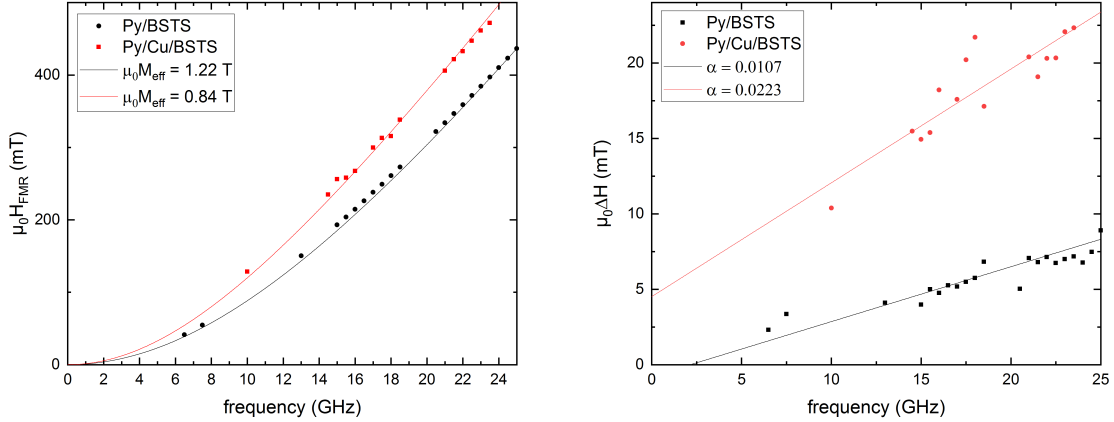


Figure 5.2: Frequency dependence of (a) H_{FMR} and (b) ΔH for the stripe-patterned Py/BSTS (black) and Py/Cu/BSTS (red) samples.

5.2 Angle dependence at room temperature

The voltage measured along the sample stripe consists of two separate effects, namely the spin-charge conversion of the topological insulator (TI) and the anisotropic magnetoresistance (AMR) effect. As described in chapter 2.5, in an FMR-experiment the precessing magnetic moments \vec{m} in the permalloy layer can accumulate spin momenta at the interface between permalloy and the topological insulator. These spin momenta can diffuse into the TI layer and cause a spin current flowing from the permalloy layer into the TI layer. The spin current is then transferred into a charge current because of spin-momentum locking in the surface states of the TI. The spin current \vec{j}_c can be described by [9] [23]

$$\vec{j}_c = A \vec{j}_s \times \vec{s}, \quad (5.1)$$

where \vec{j}_c is the charge current, \vec{j}_s is the spin current, \vec{s} is the polarisation of the spins and A is an amplitude describing the efficiency of the transfer between \vec{j}_c and \vec{j}_s . As mentioned in chapter 4.2, the sample stripe is aligned with the Y-direction of the XYZ coordinate system. Therefore at an angle $\varphi_H = 90^\circ$ the charge current caused by V_{TI} is perpendicular to the sample stripe and cannot be measured since the stripe is only contacted lengthwise. Figure 5.4 (b) illustrates the angle φ_H between the external magnetic field and the X-axis of the XYZ coordinate system. The voltage caused by V_{TI} is proportional to $\cos \varphi_H$ and has the line shape of a symmetric Lorentzian with respect to the external magnetic field. Therefore the voltage amplitude is maximal at $\varphi = 0^\circ$ and $\varphi = 180^\circ$. Different measurements of the total voltage across the sample stripe have been taken at different angles φ_H to verify this behavior.

5 Experiments

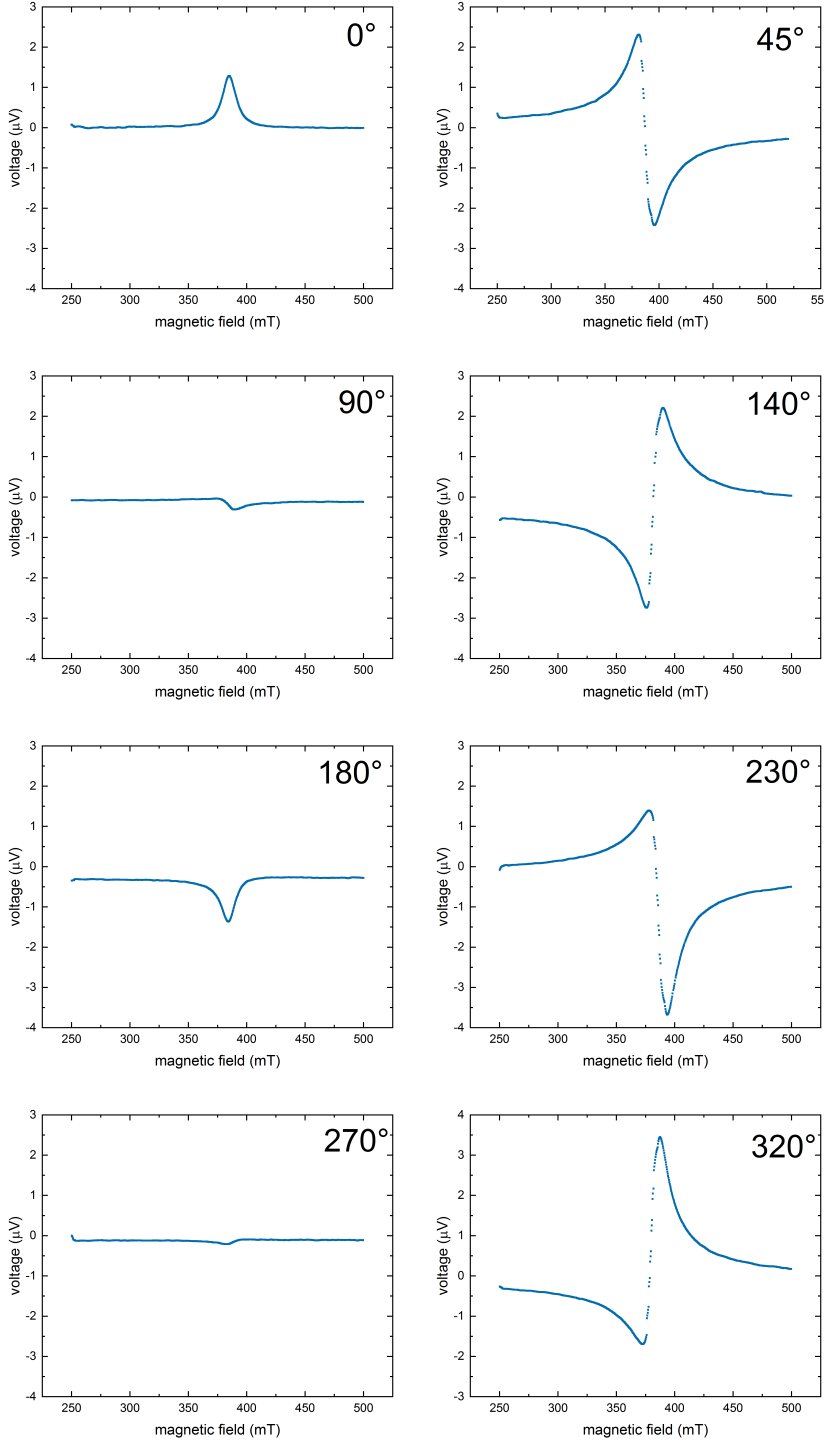


Figure 5.3: Line shapes of voltages in dependence of the external magnetic field \vec{H}_0 at different angles φ_H in a Py/Cu/BSTS stripe. For better comparison the scaling is the same for all graphs.

5.2 Angle dependence at room temperature

As can be seen in figure 5.3, the measurements at $\varphi_H = 0^\circ$ and $\varphi_H = 180^\circ$ show the expected symmetric Lorentzian line shape. Noted that the amplitude of V_{TI} changes sign between $\varphi = 0^\circ$ and $\varphi = 180^\circ$ because the external magnetic field H_0 is reversed, which causes the spin polarisation \vec{s} in equation 5.1 to change sign, and therefore the direction of the charge current changes as well.

Besides V_{TI} , the AMR effect also contributes to the voltages plotted in Fig 5.3. As mentioned in section 2.6.1 the AMR effect changes the resistance of a ferromagnet in dependence of the angle between the current flowing in the ferromagnet and the external magnetic field. The resistance is minimal for a perpendicular alignment of current and magnetic field. In an FMR-experiment inductive or capacitive coupling induce a high-frequency alternating current $I_1 \cos(\omega t)$ in the sample stripe. The magnetization in the permalloy layer, excited by the microwave magnetic field \vec{h} , is precessing with the same frequency ω . Therefore the AMR effect causes also the resistance to change with frequency ω , since the angle between current and precessing magnetization changes. Thus both the resistance and the current in the sample stripe change with ω leading to a direct voltage component in the AMR voltage V_{AMR} [16]. The line shape of V_{AMR} is the sum of a symmetric and an antisymmetric Lorentzian. The dependence of the AMR effect on the angle φ_H between the normal of the stripe and the external magnetic field can be described by $\sin(2\varphi_H)$.

Therefore at $\varphi_H = 0$ and all multiples of π the V_{TI} can be measured without the AMR effect and V_{TI} can give insight into the behavior of the topological insulator in the sample. At $\varphi_H = 45^\circ + n 90^\circ$ ($n \in \mathbb{Z}$) the AMR effect is maximal and both the amplitude of V_{TI} and V_{AMR} vanish at angles $\varphi_H = 90^\circ + n 180^\circ$ ($n \in \mathbb{Z}$). In summary figure 5.4 shows the behavior of V_{TI} and V_{AMR} dependent on the angle of the external magnetic field \vec{H}_0 to the normal of the sample stripe.

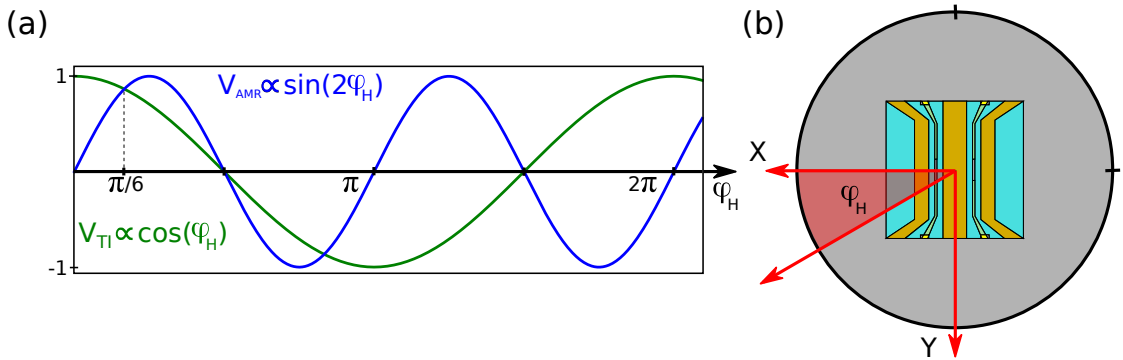


Figure 5.4: (a) Dependence of V_{TI} and V_{AMR} to the angle of the external magnetic field \vec{H}_0 . (b) Top view of the sample in the XYZ coordinate system, where the sample stripe lies in the Y direction. At $\varphi_H = 0^\circ$ the magnetic field is perpendicular to the sample stripe.

5 Experiments

As already mentioned, the voltage measurements in figure 5.3 show the expected behavior of a symmetric Lorentzian at $\varphi_H = 0^\circ$ and 180° . At $\varphi_H = 90^\circ$ and 270° a small amplitude can be seen due to minor misalignment of the external magnetic field and the sample stripe. At all the other angles both V_{TI} and V_{AMR} contribute to the voltage and therefore the sum of a symmetric and an antisymmetric Lorentzian can be observed. In order to achieve a quantitative understanding of the different voltage contributions, every measurement is fitted as described in chapter 4.4.2. The amplitudes are normalized by the power of the transmitted microwave current, which is proportional to the voltage across the Schottky diode if the microwave power is not too big. The normalized symmetric amplitude V_{sym} and antisymmetric amplitude V_{antisym} for both Py/BSTS and Py/Cu/BSTS are depicted in figure 5.5 in dependence of φ_H . The antisymmetric amplitude is roughly the same for both sample stripes. The sample stripe Py/Cu/BSTS shows a higher symmetric amplitude at $\varphi_H = 0$ of $V_{\text{sym}} = 0.44 \mu\text{V}$, whereas Py/BSTS only has $V_{\text{sym}} = 0.30 \mu\text{V}$. This increase could be explained by the decoupling between the permalloy layer and the TI by the copper layer. The copper protects the surface states from perturbation by the permalloy and therefore a higher charge current can flow in the TI. Furthermore it can be noted that the symmetric amplitudes on both sample stripes are not symmetric around 180° .

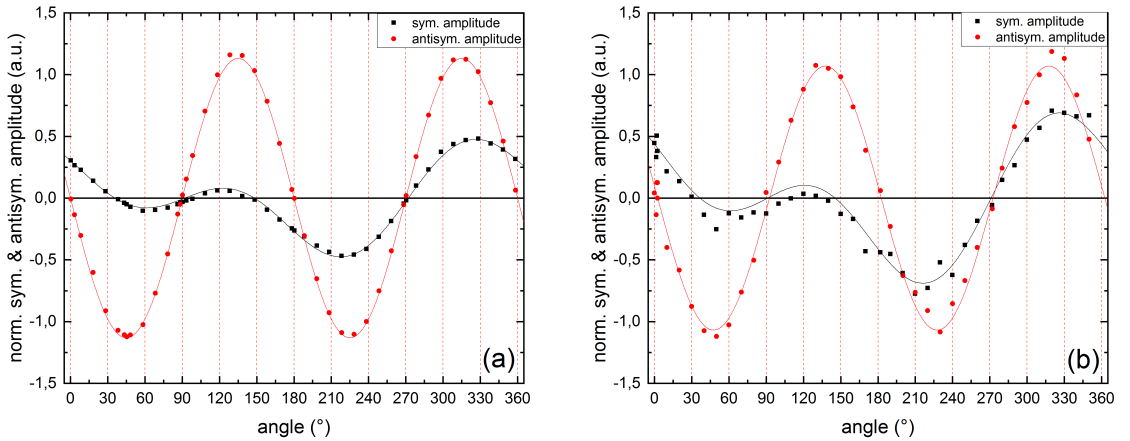


Figure 5.5: Angle dependence of (a) Py/BSTS and (b) Py/Cu/BSTS at room temperature, at microwave frequency $\omega = 23 \text{ GHz}$ and microwave power of 20 dBm.

The amplitudes in figure 5.5 have been fitted to

$$A_{\text{antisym}} = (a \sin(\varphi_H) + b) \sin(2\varphi) \quad (5.2)$$

$$A_{\text{sym}} = (c \sin(\varphi_H) + d) + e \cos(\varphi) \quad (5.3)$$

where the fit parameters a, b, c, d and e determine the physical quantities of the AMR

5.3 Temperature dependence at $\varphi_H = 45^\circ$

effect and the spin to charge conversion of the TI. The paramters are given by

$$a = A_{\text{AMR}} \text{Im}(\chi_{yy}^{\text{res}}) h_x \quad (5.4)$$

$$b = A_{\text{AMR}} \chi_{yz}^{\text{res}} h_z \sin \xi \quad (5.5)$$

$$c = A_{\text{ISHE, ip}} / 2 \quad (5.6)$$

$$d = A_{\text{AMR}} \chi_{yz}^{\text{res}} h_z \cos \xi \quad (5.7)$$

$$e = A_{\text{ISHE, oop}}. \quad (5.8)$$

A comprehensive explanation of all the fitting paramters can be found in [21]. For this thesis only the fit parameters, which have no unit, b , d and e are used, since $h_x = 0$, thus $a = 0$, and only an out-of-plane configuration is used in the experiments, thus $c = 0$. The fitting paramters for Py/BSTS yield for the antisymmetric amplitudes $b = -1.13 \cdot 10^{-6}$ and for the symmetric amplitudes $d = -2.57 \cdot 10^{-7}$ and $e = 2.86 \cdot 10^{-7}$. The fit parameter e is a measure for the spin to charge conversion in the TI. For the Py/Cu/BSTS $b = -1.07 \cdot 10^{-6}$, $d = -3.64 \cdot 10^{-7}$ and $e = 4.24 \cdot 10^{-7}$. Comparing the fitting paramters e confirms the assumption of higher spin to charge conversion in Py/Cu/BSTS.

5.3 Temperature dependence at $\varphi_H = 45^\circ$

The AMR effect is maximal at $\varphi_H = 45^\circ$ and the measured curve consists of both a symmetric and an antisymmetric part. The antisymmetric amplitude is caused only by the AMR effect, whereas the symmetric amplitude is caused by V_{AMR} and V_{TI} . The measurements at $\varphi_H = 45^\circ$ are therefore suited to investigate the AMR effect. The measured voltages at $\varphi_H = 45^\circ$ are fitted with equation 4.6. The amplitudes have to normalized before they can be interpreted. According to section 2.6.1, V_{AMR} is expressed as

$$V_{\text{AMR}} = \frac{R_A I_1 \chi_{yz}^{\text{res}} h_z}{2M_S} \left(\frac{\Delta H^2 \cos(\varphi_I)}{(H_0 - H_{\text{FMR}})^2 + \Delta H^2} - \frac{(H_0 - H_{\text{FMR}}) \sin(\varphi_I)}{(H_0 - H_{\text{FMR}})^2 + \Delta H^2} \right) \sin(2\varphi_H). \quad (5.9)$$

Since the microwave current I_1 is proportional to h_z , V_{AMR} is proportional to h_z^2 . The square of the microwave magnetic field h_z is proportional to the microwave power at the position of the sample stripe in the coplanar waveguide. Therefore the anisotropic magnetoresistance voltage has to be normalized by the microwave power. As already mentioned, the Schottky diode voltage is proportional to the transmitted microwave power and therefore V_{AMR} can be normalized by dividing through the Schottky diode voltage. Figure 5.6 shows the normalized symmetric V_{sym} and antisymmetric amplitudes V_{antisym} in dependence of the temperature.

5 Experiments

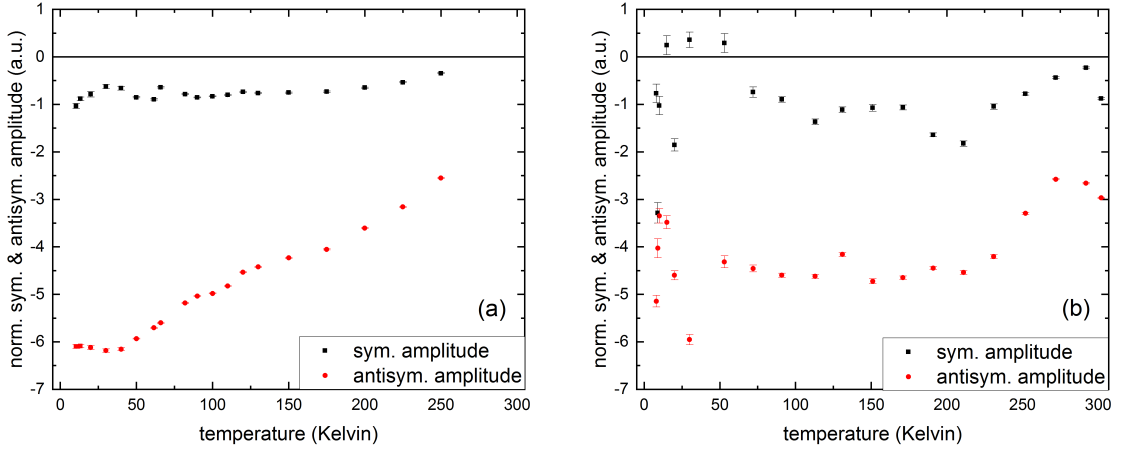


Figure 5.6: Temperature dependence at $\varphi_H = 45^\circ$ for (a) Py/BSTS and (b) Py/Cu/BSTS. The voltage amplitudes are normalized by the microwave power only.

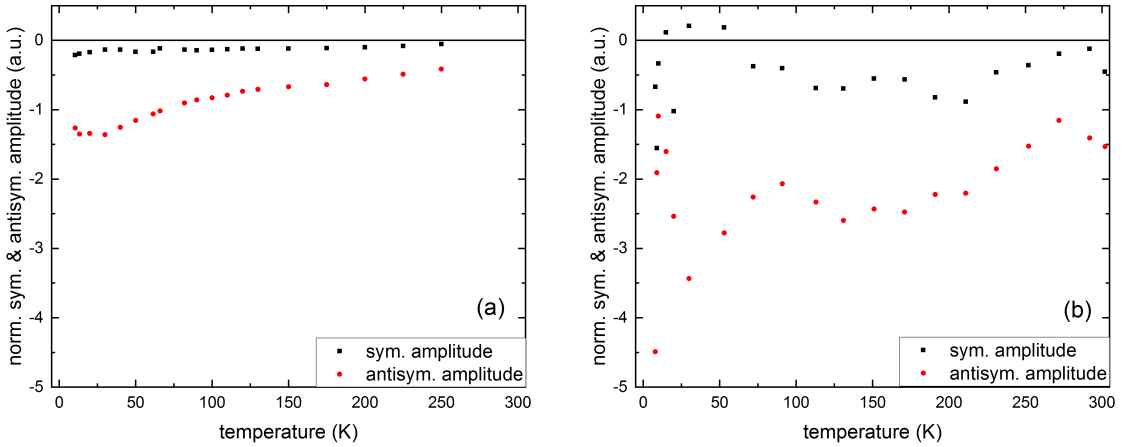


Figure 5.7: Temperature dependence at $\varphi_H = 45^\circ$ for (a) Py/BSTS and (b) Py/Cu/BSTS. The voltage amplitudes are normalized by both microwave power and the susceptibility χ_{yz}^{res} .

However, in equation 5.9 the susceptibility χ_{yz}^{res} is also dependent on the temperature. In order to examine the temperature dependence solely of the AMR effect a second normalization is necessary. According to chapter 2.4.2.5 the susceptibility χ_{yz} for $H_0 = H_{\text{FMR}}$ is given by

$$\chi_{yz}^{\text{res}} = \frac{\sqrt{\mathfrak{B}_{\text{FMR}} \mathfrak{H}_{\text{FMR}}}}{(\mathfrak{B}_{\text{FMR}} + \mu_0 \mathfrak{H}_{\text{FMR}}) \Delta H}, \quad (5.10)$$

where $\mathfrak{B}_{\text{FMR}} = \mu_0(H_{\text{FMR}} + M_{\text{eff}})$ and $\mathfrak{H}_{\text{FMR}} = H_{\text{FMR}}$. Figure 5.7 shows V_{AMR} after

5.4 Temperature dependence at $\varphi_H = 0^\circ$

being divided by χ_{yz}^{res} . Figure 5.7 (a) shows a finite symmetric amplitude, which is slowly increasing with decreasing temperature. The antisymmetric amplitude is increasing more than three times from 250 K to 30 K and has a small plateau from 30 K to 10 K. The measurements on the Py/Cu/BSTS side were difficult since the signal-noise ratio was poor especially for temperatures below 50 K. For this reason the sweeping velocity of the external magnetic field was lowered, in order to increase the measuring points. This broadened the measured voltage curves as can be seen in figure 5.9. For temperatures from 200 K to 300 K a decrease of the antisymmetric amplitude can be seen. Between 100 K and 200 K V_{antisym} is approximately constant.

5.4 Temperature dependence at $\varphi_H = 0^\circ$

For $\varphi_H = 0^\circ$ the AMR effect is zero and therefore the voltage signal generated by the topological insulator can be studied exclusively. Since V_{AMR} is zero, the measured voltage curves are expected to be a symmetric Lorentzian with a zero antisymmetric amplitude. The measured amplitudes have to be normalized by the microwave power. This is accomplished by dividing the amplitudes by the Schottky diode voltage. Figure 5.8 shows the symmetric and antisymmetric amplitudes for different temperatures.

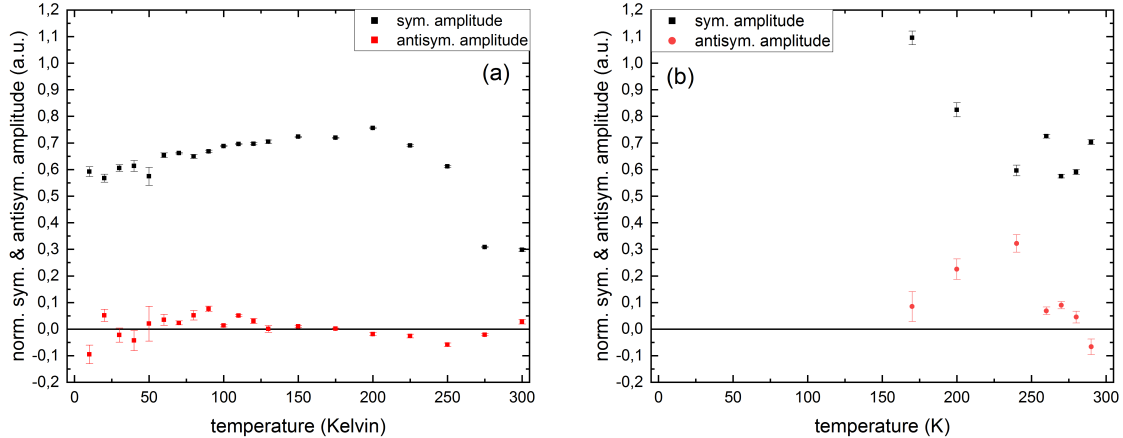


Figure 5.8: Temperature dependence of the voltage measured along the stripe at $\varphi_H = 0^\circ$ for (a) Py/BSTS and (b) Py/Cu/BSTS.

Figure 5.8 (a) shows a vanishingly small antisymmetric amplitude for the Py/BSTS side at $\varphi_H = 0^\circ$. The symmetric amplitude V_{sym} increases considerably from 300 K to 200 K. This increase of the symmetric amplitude cannot be explained at this point. The symmetric amplitude then declines from $V_{\text{sym}} = 0.76$ at 200 K to 0.59 at 10 K. The

5 Experiments

surface states of a topological insulator are especially prominent at low temperatures since the bulk carriers of the TI tend to *freeze-out* [4]. Therefore a possible explanation for the decline of V_{sym} from 200 K to 10 K could be the removal of the bulk conductivity in the TI. For the Py/Cu/BSTS side no signal can be detected below 170 K. The symmetric amplitude increases considerably for temperatures from 300 K to 170 K on the Py/Cu/BSTS side, which may indicate the decoupling effect of the copper layer. Figure 5.9 (a) shows the measured voltage along the stripe for different temperatures on the Py/BSTS side. The signal has as expected a symmetric Lorentzian line shape and increases with decreasing temperature from 300 K to 10 K. Figure (b) shows the normalized measured voltage along the stripe for different temperatures.

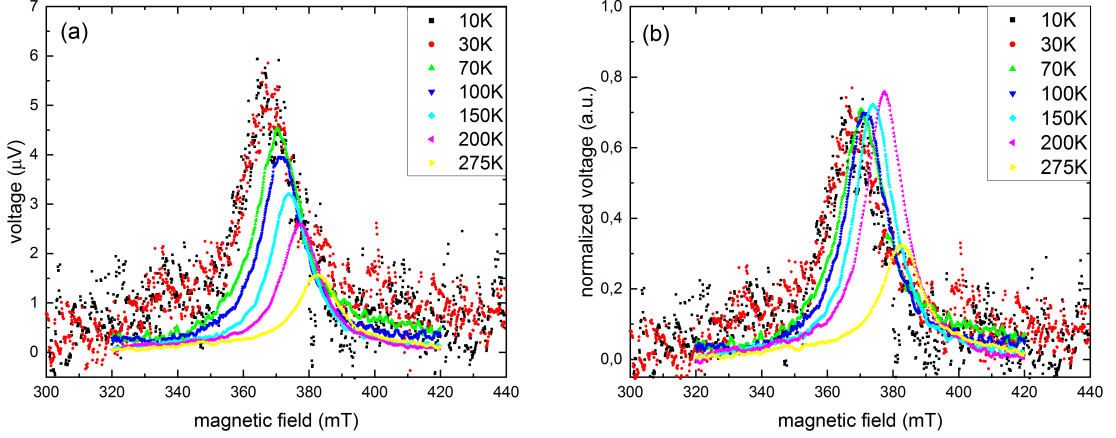


Figure 5.9: Voltage line shapes at different temperatures at the Py/BSTS side at $\varphi_H = 0$.
 (a) Symmetric amplitude without normalization by the microwave power.
 (b) Symmetric amplitude with normalization by the microwave power. In both figures an offset was applied to the measured curves for better visual comparison of the symmetric amplitudes V_{sym} .

5.5 Angle dependence for Py/BSTS at room temperature and 10 Kelvin

In addition to the angle dependent measurement at room temperature in chapter 5.2, an additional angle dependent measurement for Py/BSTS has been performed at 10 K. Figure 5.10 shows the measurement results of chapter 5.2 on Py/BSTS (a) at room temperature in comparison to (b) at 10 K. The symmetric and antisymmetric amplitudes are fitted by equation 5.2 and again normalized by the microwave power. As already mentioned the fit parameters for room temperature are $b = -1.13 \cdot 10^{-6}$, $d = -2.57 \cdot 10^{-7}$ and $e = 2.86 \cdot 10^{-7}$. For 10 K $b = -6.00 \cdot 10^{-6}$, $d = -1.15 \cdot 10^{-6}$ and $e = 4.50 \cdot 10^{-7}$.

5.5 Angle dependence for Py/BSTS at room temperature and 10 Kelvin

The parameter e is describing the voltage due to spin pumping into the TI and is almost 57% higher for 10 K, which indicates a more efficient spin to charge conversion than at room temperature. At $\varphi_H = 0^\circ$ the symmetric amplitude increased from $V_{\text{sym}} = 0.31$ at room temperature to $V_{\text{sym}} = 0.59$ at 10 K. The antisymmetric amplitude V_{antisym} at $\varphi_H = 45^\circ$ has increased from 1.13 at room temperature to 6.00 at 10 K.

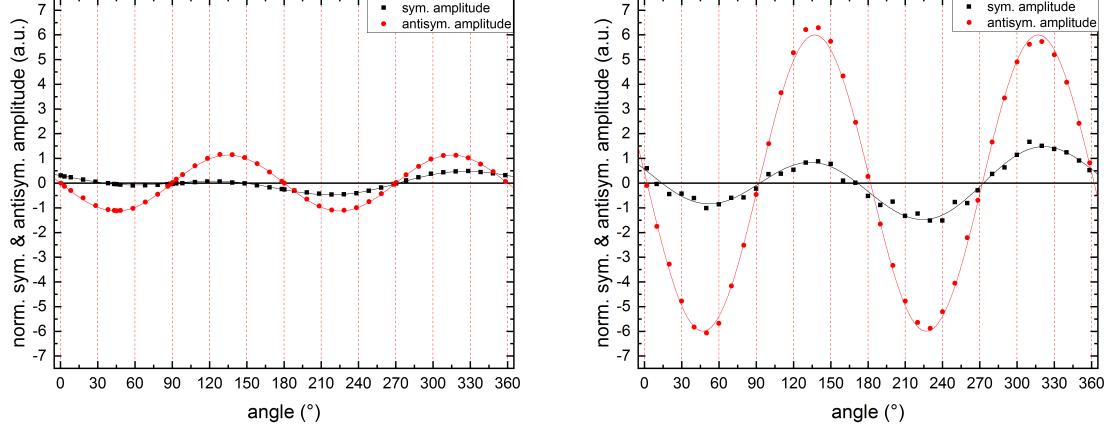


Figure 5.10: Angle dependence for Py/BSTS at (a) room temperature and (b) 10 K. At $\varphi_H = 0^\circ$ the symmetric amplitude V_{sym} at 10 K has increased by 90% in comparison to the measurement at room temperature. At $\varphi_H = 45^\circ$ the antisymmetric amplitude V_{antisym} has increased by more than five times in comparison to the measurement at room temperature. The symmetric and antisymmetric amplitudes are normalized by the microwave power.

6 Conclusion

The objective of this thesis was the confirmation of the existance and investigation of surface states in a topological insulator. For this reason a sample was fabricated, where on one half of the sample a bilayer structure of permalloy Py and topological insulator BSTS was grown and on the other half a trilayer structure of Py, copper Cu and BSTS was grown. The idea was that the copper layer acts as a decoupling layer between permalloy and the TI, which could lead to a more efficient spin to charge conversion in the TI. Therefore to find a suitable sample FMR measurements were performed on various samples with different materials for the substrate, the paramagnetic and the ferromagnetic layer with varying thicknesses. In the end a sample with a Al_2O_3 substrate, 10 nm thick Py layer, 5 nm thick Cu layer and a layer of the topoligical insulator BiSbTeSe with a thickness of 10 quintuple layers was picked because the sample showed an increased damping factor for the Py/Cu/BSTS side in the fullfilm FMR measurement. An increased damping factor can be a consequence of more efficient spin to charge conversion due to surface states of the topological insulator. Optical lithography was used to fabricate a CPW onto the sample in order to perform an out-of-plane FMR-experiment in the cryostat setup. Furthermore the voltage across the sample stripe could be measured in dependence to the angle of the external magnetic field to the sample stripe. The voltage consisted of two contributions, namely the spin to charge conversion of the TI and the anisotropic magnetoresistance of the permalloy. By performing an angle dependent measurement of both Py/BSTS and Py/Cu/BSTS an increase of the symmetric amplitude in Py/Cu/BSTS in respect to Py/BSTS could be detected at $\varphi_H = 0^\circ$. At this angle the symmetric amplitude consists only of the voltage caused by the TI. At the angle $\varphi_H = 45^\circ$ a temperature dependent measurement was performed. The voltage measurements for the Py/BSTS showed as expected a finite symmetric amplitude with an maximum antisymmetric amplitude. The antisymmetric amplitude increased considerably with decreasing temperature. The measurement of Py/Cu/BSTS at low temperatures were inconclusive due to a low signal-noise ratio. The temperature dependent measurements at $\varphi_H = 0^\circ$ showed as expected a vanishingly small antisymmetric amplitude. The symmetric amplitude is increasing up to 200 K and for temperatures below 200 K the symmetric amplitude is decreasing slowly. The bulk carriers of the TI are expected to *freeze-out* at low temperatures, which could be a reason for the decreasing symmetric amplitude for 200 K to 10 K. A comparison of a angle dependent measurement of Py/BSTS between room temperature and 10 K showed a strongly increased maximum antisymmetric amplitude and an almost twice as large symmetric amplitude.

Whether the symmetric amplitude V_{sym} at φ_H was caused by spin-momentum locking of the surface states in the TI cannot be answered with certainty. The increase of the fit parameter e and the symmetric amplitude V_{sym} in Py/Cu/BSTS are promising but further experiments have to be performed. For example a thickness dependent measurement of the topological insulator would be useful. Under the assumption that only the surface states of the TI contribute to the spin to charge conversion a thicker layer of a topological insulator should not increase the charge current across the sample stripe in an FMR-experiment. Fabricating two or three of these samples with a consistent composition of the TI however is difficult.

Bibliography

- [1] Anton Akhmerov et al. *Topology in Condensed Matter*. 2015. URL: <https://topocondmat.org/>.
- [2] A Azevedo et al. “Spin pumping and anisotropic magnetoresistance voltages in magnetic bilayers: Theory and experiment”. In: *Physical review B* 83.14 (2011), p. 144402.
- [3] Stephen Blundell. *Magnetism in condensed matter*. 2003.
- [4] E Burstein et al. *Series Preface Contemporary concepts of condensed matter science: Board of Editors*. 2008.
- [5] Z Celinski, KB Urquhart, and B Heinrich. “Using ferromagnetic resonance to measure the magnetic moments of ultrathin films”. In: *Journal of Magnetism and Magnetic Materials* 166.1-2 (1997), pp. 6–26.
- [6] John MD Coey. *Magnetism and magnetic materials*. Cambridge university press, 2010.
- [7] Martin Decker. “Spin Current Induced Control of Magnetization Dynamics”. Dissertation. University of Regensburg, Department of Physics, 2017.
- [8] Wolfgang Demtröder. *Experimentalphysik*. Vol. 2. Springer, 1995.
- [9] Z Feng et al. “Spin Hall angle quantification from spin pumping and microwave photoresistance”. In: *Physical Review B* 85.21 (2012), p. 214423.
- [10] F Duncan M Haldane. “Model for a quantum Hall effect without Landau levels: Condensed-matter realization of the "parity anomaly"”. In: *Physical review letters* 61.18 (1988), p. 2015.
- [11] Markus Härtinger. “Magnetische Eigenschaften neuer ferromagnetischer Materialien”. Master thesis. University of Regensburg, Department of Physics, 2011.
- [12] M Zahid Hasan and Charles L Kane. “Colloquium: topological insulators”. In: *Reviews of modern physics* 82.4 (2010), p. 3045.
- [13] Charles Kittel. “On the theory of ferromagnetic resonance absorption”. In: *Physical Review* 73.2 (1948), p. 155.
- [14] LALE Landau and Evgeny Lifshitz. “On the theory of the dispersion of magnetic permeability in ferromagnetic bodies”. In: *Perspectives in Theoretical Physics*. Elsevier, 1992, pp. 51–65.

Bibliography

- [15] John M Lee. *Riemannian manifolds: an introduction to curvature*. Vol. 176. Springer Science & Business Media, 2006.
- [16] Thomas Meier. “Temperaturabhängige Messungen des inversen Spin-Hall-Effekts”. Bachelor’s thesis. University of Regensburg, Department of Physics, 2012.
- [17] Joel E Moore. “The birth of topological insulators”. In: *Nature* 464.7286 (2010), p. 194.
- [18] O Mosendz et al. “Quantifying spin Hall angles from spin pumping: Experiments and theory”. In: *Physical review letters* 104.4 (2010), p. 046601.
- [19] JP Nibarger et al. “Variation of magnetization and the Landé g factor with thickness in Ni–Fe films”. In: *Applied physics letters* 83.1 (2003), pp. 93–95.
- [20] Wolfgang Nolting and Wolfgang Nolting. *Grundkurs Theoretische Physik 1: Klassische Mechanik*. Vol. 6. Springer, 2006.
- [21] Martin Obstbaum. “Inverse spin Hall effect in metallic heterostructures”. Dissertation. University of Regensburg, Department of Physics, 2015.
- [22] Xingyue Peng et al. “Spin generation via bulk spin current in three-dimensional topological insulators”. In: *Nature communications* 7 (2016), p. 10878.
- [23] E Saitoh et al. “Conversion of spin current into charge current at room temperature: Inverse spin-Hall effect”. In: *Applied physics letters* 88.18 (2006), p. 182509.
- [24] Kai Sun. *Advanced Condensed Matter Physics*. 2013. URL: http://www-personal.umich.edu/~sunkai/teaching/Fall_2013/chapter7.pdf.
- [25] Yaroslav Tserkovnyak, Arne Brataas, and Gerrit EW Bauer. “Enhanced Gilbert damping in thin ferromagnetic films”. In: *Physical review letters* 88.11 (2002), p. 117601.
- [26] Yaroslav Tserkovnyak, Arne Brataas, and Gerrit EW Bauer. “Spin pumping and magnetization dynamics in metallic multilayers”. In: *Physical Review B* 66.22 (2002), p. 224403.
- [27] M Mitchell Waldrop. “The chips are down for Moore’s law”. In: *Nature News* 530.7589 (2016), p. 144.
- [28] Georg Woltersdorf. “Spin-Pumping and Two-Magnon-Scattering in Magnetic Multilayers”. Dissertation. University of Regensburg, Department of Physics, 2004.

Acknowledgments

Ich möchte mich bei Prof. Dr. Christian Back herzlich für die Themenstellung und die Betreuung bedanken.

Vielen Dank an meine beiden Betreuer, Dr. Matthias Kronseder und Thomas Maier, für die tatkräftige Unterstützung.

Ein großer Dank geht an den kompletten Lehrstuhl. Es war mir eine große Freude mit euch an so vielen Feiern und Ausflügen teilgenommen zu haben. Meine Highlights dabei waren Hausboot fahren, die Weihnachtsfeiern oder das Pizza-Feast, um nur ein paar zu nennen.

Meine beiden Bürokollegen, Thomas Meier und Michael „Zippo“ Zimmermann, hätte ich mir besser nicht aussuchen können. Dank eurer Unterstützung stehen mir die Berufszweige des Pizzabäckers und Dartprofis nach meinem Studium weit offen.

Ich habe die Arbeit selbständig verfasst, keine anderen als die angegebenen Quellen und Hilfsmittel benutzt und bisher keiner anderen Prüfungsbehörde vorgelegt. Außerdem bestätige ich hiermit, dass die vorgelegten Druckexemplare und die vorgelegte elektronische Version der Arbeit identisch sind, dass ich über wissenschaftlich korrektes Arbeiten und Zitieren aufgeklärt wurde und dass ich von den in § 24 Abs. 5 vorgesehenen Rechtsfolgen Kenntnis habe.

Regensburg, 30th of September 2019
